Separating cognitive and motor processes in the behaving mouse

Munib A. Hasnain[1,3*], Jaclyn E. Birnbaum[2,3*], Juan Luis Ugarte Nunez[1], Emma K. Hartman[1], Chandramouli Chandrasekaran[4,5,6], Michael N. Economo[1,3,6#]

[*] These authors contributed equally. Order determined via coin flip.

[#] Corresponding author

Email: mne@bu.edu

[1] *Department of Biomedical Engineering, Boston University, Boston, MA*

[2] *Graduate Program for Neuroscience, Boston University, Boston, MA*

[3] *Center for Neurophotonics, Boston University, Boston, MA*

[4] *Department of Psychological and Brain Sciences, Boston University, Boston, MA*

[5] *Department of Neurobiology & Anatomy, Boston University, Boston, MA*

[6] *Center for Systems Neuroscience, Boston University, Boston, MA*

Abstract

The cognitive processes supporting complex animal behavior are closely associated with ubiquitous movements responsible for our posture, facial expressions, ability to actively sample our sensory environments, and other central processes. These movements are strongly related to neural activity across much of the brain, making it challenging to dissociate the neural dynamics that support cognitive processes from those supporting movements when they are highly correlated in time. Of critical importance is whether the dynamics supporting cognitive processes and related movements are separable, or if they are both driven by common neural mechanisms. Here, we demonstrate how the separability of cognitive and motor processes can be assessed, and, when separable, how each component can be isolated. We establish a novel two-context behavioral task in mice that involves multiple cognitive processes and show that commonly observed dynamics taken to support cognitive processes are strongly contaminated by movements. When cognitive and motor components are isolated using our analytical approach, we find that they exhibit distinct dynamical trajectories. Further, properly accounting for movement revealed that separate populations of cells encode cognitive and motor variables, in contrast to the 'mixed selectivity' reported by prior work. Accurately isolating the dynamics associated with particular cognitive and motor processes will be essential for developing conceptual and computational models of neural circuit function and evaluating the function of the cell types of which neural circuits are composed.

Introduction

Goal-directed behavior follows from an interplay between cognitive and motor processes in the mammalian brain. For example, while dribbling down the court, a basketball player must track the players around them, decide which play to run, plan their next move, execute fast and accurate movements, and flexibly adapt their movements according to the reactions of other players. The neural representations of these cognitive and motor processes are often distributed across many of the same brain areas[1–6] and engaged concurrently[7–9]. For these reasons, disentangling the neural signatures of specific cognitive and motor processes is challenging.

Many behavioral tasks are designed with this issue in mind, aiming to isolate constituent neural processes by separating them into discrete temporal epochs. For example, in sensory-guided decision-making tasks, subjects are often trained to withhold responses while stimuli are presented so that perceptual decision making is isolated in time from associated actions. Analogous paradigms have been developed to uncover the neural underpinnings of working memory[10–12], motor planning[13,14], contextual encoding[15,16], reward prediction[17,18], and other cognitive processes[19–22].

These paradigms often rely on the assumption that experimental subjects withhold motor output during task epochs in which instructed responses are absent. However, uninstructed movements not required for task completion – such as changes in posture, facial expressions, and gaze – are commonly observed in rodents, humans, and non-human primates during learned behavioral tasks[23–29]. Importantly, uninstructed movements explain much of the variance observed in brain-wide neural activity[27,30–32] and can be strongly correlated with task variables[12,28,33–38].

These observations imply a serious challenge for experimental studies addressing a wide-ranging set of cognitive processes. If uninstructed movements are correlated with a latent cognitive variable of interest – a stimulus perceived, a decision made, a memory stored, or a motor plan formed – then the neural dynamics leading to, or resulting from, uninstructed movements can be easily misconstrued as responsible for that cognitive process. One common approach to isolate putative cognitive dynamics is to measure and 'regress out' movements[24,30,39–44], but this approach assumes that cognitive and motor processes are driven by independent neural dynamics. Some cognitive processes may be inherently embodied, such that their associated neural dynamics are linked to overt movement[45,46]. Regressing out neural dynamics associated with embodied movements would lead to the inadvertent removal of the precise dynamics one wishes to study. Whether cognitive and motor dynamics are separable remains an open question and likely depends on the brain area, behavior, and cognitive process of interest. Methods both for evaluating separability within specific experimental paradigms and for effectively dissociating cognitive and motor dynamics, when separable, are lacking.

Here, we address the separability of dynamics associated with cognitive processes (defined broadly here as those not directly related to motor commands, efference copies, or sensory reafference) and correlated movements. We developed a behavioral paradigm in which mice perform sensory-guided movements involving multiple cognitive signals and idiosyncratic, task-correlated uninstructed movements. We build upon work showing that different neural processes can be multiplexed in a single brain region[39,40,47–50] to develop a novel method for assessing the separability of cognitive and motor dynamics – and for isolating each component, when they are separable. This approach is simple to adopt and model-free, precluding the need for parameter adjustment or assumptions of linearity.

We find that some cognitive signals are separable from dynamics associated with co-occurring movements while others are largely inseparable. When dynamics are separable, examining the 'cognitive' component of neural dynamics revealed trajectories that differed markedly from estimates of the same dynamics when corrupted by uninstructed movements. Strikingly, we found that cognitive and motor variables were largely encoded by separate populations of cells, in contrast to previous work that did not account for uninstructed movements. Together, these results highlight the importance of critical consideration of the relationship between cognition and movements to better understand the neural dynamics supporting complex processes and how they map onto the myriad cell types comprising neural circuits.

Results

Task-switching behavioral paradigm

We first designed a behavioral paradigm associated with multiple cognitive processes. In this paradigm, head-fixed mice performed two directional licking tasks that alternated block-wise within each behavioral session. These tasks varied in their cognitive demands but require the same instructed motor output.

This paradigm employed an established delayed-response task (DR) in which motor planning is temporally dissociated from movement execution (**Fig. 1a**). In this task, an auditory stimulus indicated the location of a reward. After a brief delay epoch, an auditory 'go cue' instructed the mouse to move. If the mouse performed a directional tongue movement to the correct target, a water reward was delivered. In separate blocks of trials, mice performed a water-cued (WC) task in which all auditory stimuli were omitted. Instead, a drop of water was presented at a random point in time at a randomly selected reward port. Animals consumed water immediately upon its presentation. Mice received no explicit cues signaling DR and WC blocks. The DR task required a perceptual decision that guides the planning of a subsequent motor action. In the WC task, uncertainty in the timing and location of reward prevented formation of a motor plan prior to reward presentation, and instead, mice detected reward availability using olfactory and/or vibrissal cues[51]. This structure required animals to maintain a representation of the current block identity (context) for successful task execution.

We examined uninstructed movements in this behavioral paradigm using high-speed video. We tracked movement of the tongue, jaw, nose, and paws[52] and calculated frame-by-frame motion energy to quantify movement in a feature-agnostic manner[31] (**Fig. 1d-f**). We found that mice performed uninstructed movements in both contexts that varied in both their identity and timing across trials and contexts (**Fig. 1e; Supplementary Movie 1**).

Prior work has established the necessity of the antero-lateral motor cortex (ALM) and tongue-jaw motor cortex (tjM1) for the planning and execution of tongue movements[14,53–56]. To assess cortical involvement in the initiation of instructed movements (directional licking) in both behavioral tasks, we used optogenetic photoinactivation to inhibit the ALM and tjM1 at the go cue (DR) or water presentation (WC) bilaterally in VGAT-ChR2-EYFP mice (2 mice, 6 sessions). Simultaneous photoinactivation of both regions at the go cue impaired the initiation of movement in both contexts (**Fig. 1b,c**; DR left trials: $p = 4\text{x}10^{-5}$, DR right trials: $p = 0.02$, WC left trials: $p = 0.02$, WC right trials: $p = 0.04$, paired *t*-test; **EDFig. 1c,d**). To assess cortical involvement in the expression of uninstructed movements, we bilaterally silenced the ALM and tjM1 during the delay epoch of DR trials (2 mice, ALM: 15 sessions, tjM1: 9 sessions). Uninstructed movements were suppressed by photoinactivation of either area (**EDFig. 1b,** ALM: p=3x10^{-4}; tjM1: p=0.002, paired *t*-test) and more strongly suppressed by concurrent photoinactivation of both areas (**Fig. 1g-h,** 2 mice, 14 sessions; p=3x10^{-7}), similar to previous observations[34] (but see ref[57]). In the DR task, delay photoinactivation of both areas led to a significant decrease in overall performance (**Fig. 1i**, All trials: p=0.002, paired *t*-test; and **EDFig. 1b**) as expected from the disruption of choice/planning dynamics[14]. These results indicate that the ALM and tjM1 are involved in the generation of uninstructed movements and the planning and execution of instructed directional tongue movements in the two-context paradigm.

Neural dynamics related to task variables

While movement- and task-related information are encoded in both the ALM and tjM1 in the DR task[53,58] and other directional licking tasks[55], task variables are more strongly represented in the ALM[55,56,59] and so we focused our subsequent analyses there. We recorded activity extracellularly in the ALM with high-density silicon probes during the two-context paradigm to track dynamics associated with planning, context, and the execution of movements (**Fig. 2**; DR task only: 9 mice, 25 sessions, 1651 units including 483 well-isolated single units; task switching (DR and WC tasks): 6 mice, 12 sessions, 522 units including 214 well-isolated single units). As reported previously, we found that choice selectivity (right vs. left DR trials) was widespread across all task epochs (sample: 36%, delay: 42%, response: 58% of single units; 9 mice, 483 single units). Individual units showed a variety of activity patterns across trial types, including delay epoch preparatory activity preceding

instructed movements, a key signature of motor planning[54] (**Fig. 2b,** *left*). Individual units were also selective for behavioral context during all task epochs

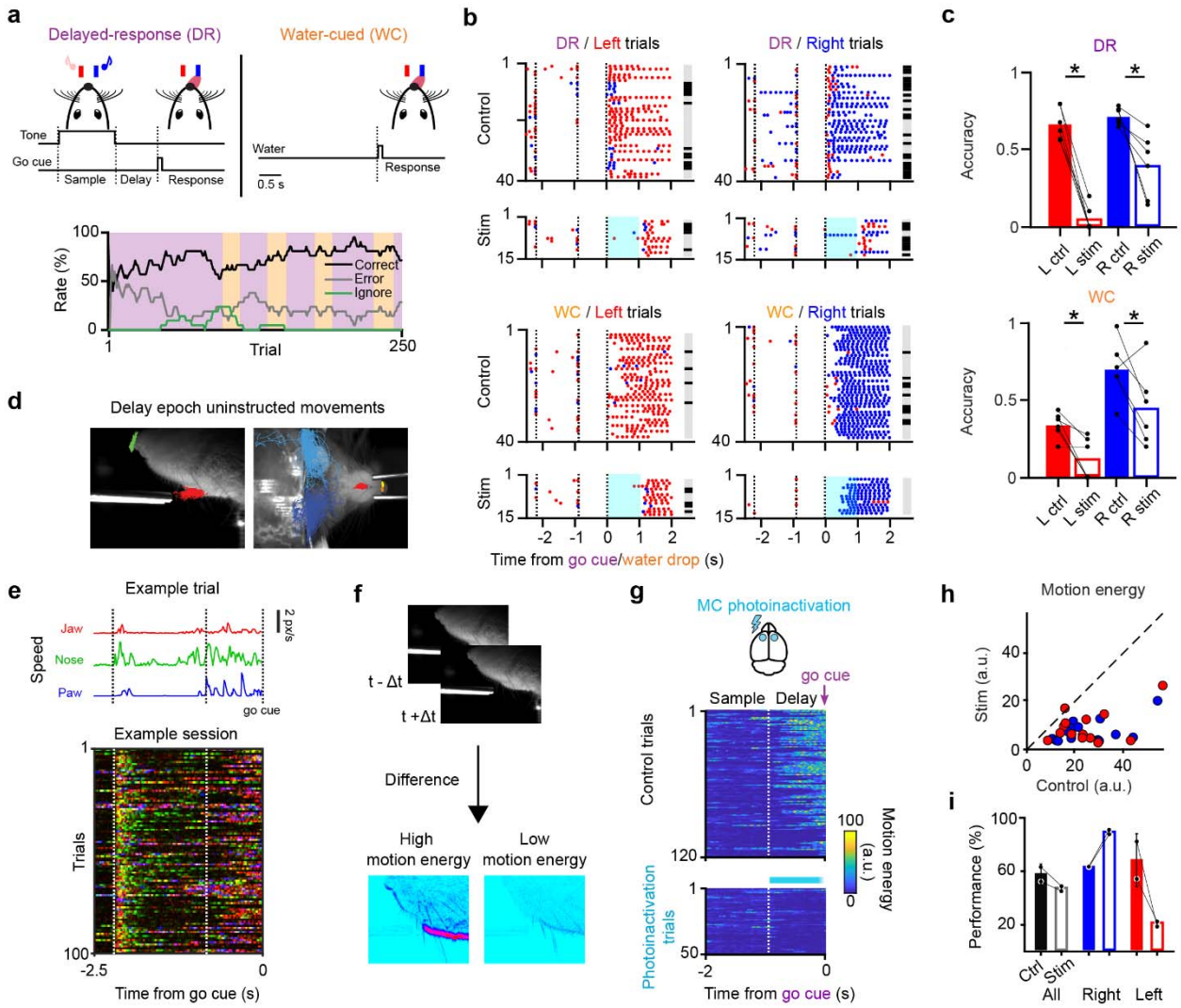

Figure 1 – Cortical dependence and uninstructed movements during a two-context task. a. *Top*, Schematic of the two-context task. In delayed-response (DR) trials, an auditory stimulus was presented during the sample epoch (1.3 s) instructing mice to lick for reward to the right (white noise) or left (pure tone). Mice were trained to withhold their response during a delay epoch (0.9 s) and initiated their response following an auditory go cue. In WC trials, mice were presented with a water reward at a random port at random inter-reward intervals. The WC task was introduced once mice became experts in the DR task. *Bottom*, 20-trial trailing average of correct, error, and ignore rates for an example session. **b.** Performance for an example session separated by trial type (left vs. right), control vs. photoinactivation trials, and by context. Photoinactivation (1 s) was initiated at the go cue. Blue dots indicate right licks and red dots indicate left licks. Grey bars, correct trials; black bars, error trials. **c.** Proportion of trials with correct licks within 600 ms of the go cue on photoinactivation trials. Each point indicates mean value for a session. *Top*, DR context. *Bottom*, WC context. Asterisks denote significant differences ($p < 0.05$) between control and photoinactivation trials (DR left trials: $p = 4\text{x}10^{-5}$, DR right trials: $p = 0.02$, WC left trials: $p = 0.02$, WC right trials: $p = 0.04$, *paired t-test*). **d.** Behavior was tracked with high-speed video from side (*left*) and bottom (*right*) views. **e.** Trajectories of delay epoch uninstructed movements from an example session overlayed. Uninstructed movements are highly variable across trials and across time. *Top*, jaw, nose, and paw speed for an example trial. *Bottom*, feature overlay for a subset of trials in an example session. At each time bin, *t*, an [r, g, b] color value was encoded as [jaw_t ,nose_t ,paw_t]. **f.** Schematic of motion energy calculation. Example frames depicting high and low motion energy are shown. **g-i.** Bilateral motor cortex photoinactivation during the delay epoch (n=2 mice). **g.** Motion energy on control (*top*) and photoinactivation (*bottom*) trials for an example session. On photoinactivation trials, light was delivered for 0.8 seconds beginning at the start of the delay epoch. **h.** Average delay epoch motion energy on single sessions for control and photoinactivation trials. Red points indicate left trials and blue points indicate right trials for a single session. **i.** Performance for control and delay epoch

photoinactivation trials. Mice revert to a default choice following delay epoch photoinactivation. Each point indicates average performance over all sessions for each mouse. Error bars indicate standard deviation across all sessions.

and during the inter-trial interval (ITI) (26% of single units; 6 mice, 214 single units), suggesting persistent coding of context (**Fig. 2b,** *right*).

We next sought to understand how the selectivity patterns observed in individual cells were encoded at the population level. We examined neural activity in state space, in which the firing rate of each unit represents one dimension. We defined one-dimensional coding directions (CD) within the high-dimensional state space that best encoded task variables[54,60–62] (**Fig. 2c**). We first examined putative neural correlates of three cognitive processes – choice, urgency, and contextual encoding.

We defined a coding direction for left-right trial type, CD_{choice}, as the direction in state space that best differentiates activity on left versus right trials during the delay epoch of DR trials. Projections along CD_{choice} revealed that choice selectivity in the ALM emerges early in the sample epoch and continues to grow throughout the delay epoch before collapsing at the onset of the response epoch (**Fig. 2d**). Such preparatory activity is predictive of animals' upcoming instructed responses[13,54,58,60,63,64] and has been taken to represent a neural correlate of a motor plan[54,65] or choice[32,61,66]. We next defined CD_{ramp} as the direction that captures trial-type independent increases or decreases in preparatory activity between the onset of the stimulus and the go cue in DR trials[60,61,67,68]. This non-selective ramping has been thought to represent an urgency (or timing) signal[69–72]. Finally, we defined $CD_{context}$, the direction that best differentiates activity on DR and WC trials during inter-trial intervals. Projections along $CD_{context}$ revealed that context is encoded in the ALM throughout each trial (**Fig. 2d**) with strong modulation at the onset of the response epoch.

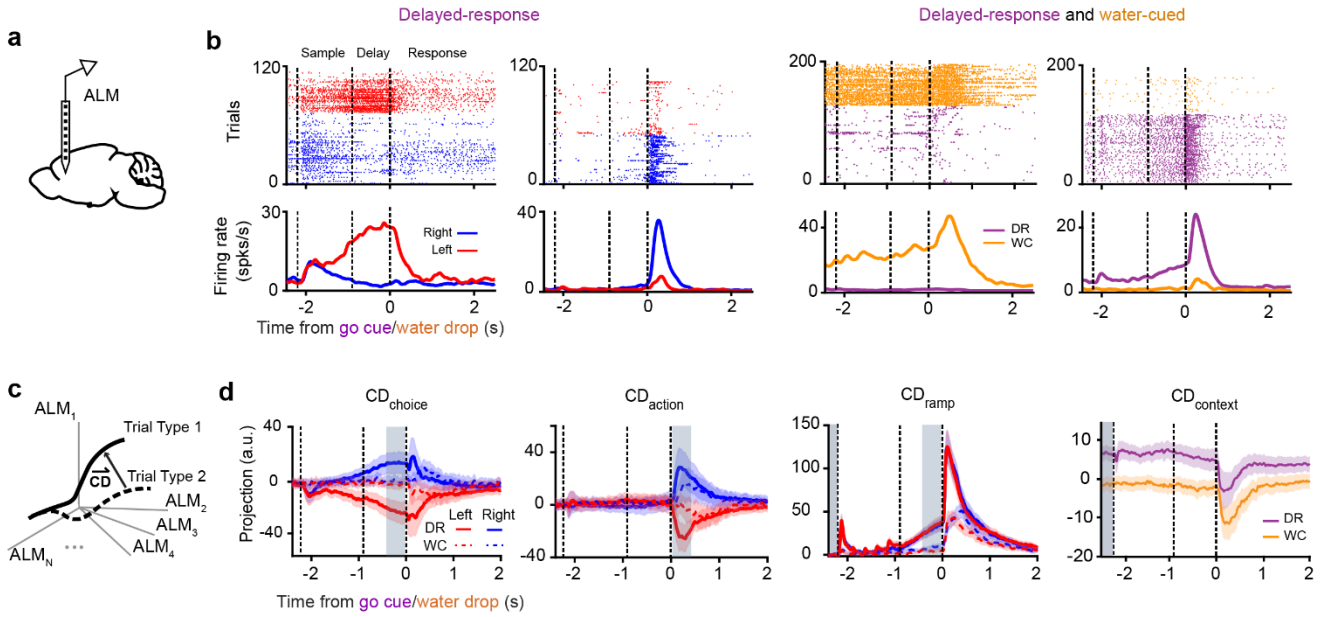

Figure 2 – Single cell activity and population dynamics encode task-relevant cognitive and motor processes. Schematic of silicon probe recordings in the anterolateral motor cortex (ALM). **b.** Spike rasters (*top*) and peri-stimulus time histograms (PSTH; *bottom*) for four example units in the ALM. Units show selectivity for trial type (left vs. right) and context (DR vs. WC) during all task epochs. **c.** Schematic illustrating identification of coding directions (CD). Coding directions are defined as directions in state space that maximally separate activity between trajectories defined by trial types (CD_{choice}, CD_{action}), context ($CD_{context}$), or time points (CD_{ramp}). **d.** Projections along each of four defined CDs. Gray shaded regions indicate time points used for CD estimation. Mean and 95% CI of bootstrap distribution shown.

In addition to neural activity putatively related to these cognitive processes, we also examined neural signals associated with the execution of movements. We defined an additional coding direction, CD_{action}, as the direction that captures trial-type selective changes in neural activity that emerge after the go cue. Projections of neural activity along CD_{action} robustly encoded movement direction in the ALM, as expected. We focus our analyses on these four population level signals, which putatively encode ALM dynamics associated with cognitive and motor processes in the two-context task-switching paradigm.

Uninstructed movements related to preparatory dynamics

We next examined uninstructed movements in the DR task and their correlation with both task variables and preparatory dynamics (**Fig. 3**). We found that animals frequently performed uninstructed movements that were correlated with trial type (**Fig. 3a**) and time within each trial. On single trials, upcoming choice could be decoded from uninstructed movements beginning immediately after the presentation of the sample tone, with accuracy increasing throughout the delay epoch (**Fig. 3b**).

Not only were uninstructed movements related to the animal's upcoming actions, but they were highly correlated with preparatory dynamics. The onset and magnitude of uninstructed movements coincided with the onset and magnitude of choice selectivity and ramping (**Fig. 3c,e**). We used cross-validated multiple linear regression to predict projections along CD_{choice} and CD_{ramp} on a trial-by-trial basis from captured kinematic features. Model predictions were often highly correlated with motor planning signals, indicating a close relationship between animals' uninstructed movements and preparatory dynamics (**Fig. 3d,f**; CD_{choice}: $R^2 = 0.41 \pm 0.23$; CD_{ramp}: $R^2 = 0.48 \pm 0.23$), although a high degree of variability was observed in the features that were most predictive across animals and sessions (**EDFig. 2a-c**).

To further understand the relationship between uninstructed movements and preparatory dynamics, we trained additional animals on a randomized delay task in which the timing of the go cue cannot be anticipated[64]. Incorporating uncertainty into the length of the delay epoch leads to a qualitative change in population-level choice selectivity; selectivity at both the single-neuron level and in CD_{choice} projections emerges earlier than in the standard DR task and ramps up to a stable fixed point, suggesting that motor plans are prepared prior to the earliest possible go cue time[64] (**Fig. 3g,** *middle*). We found that the timing of uninstructed movements, too, shifted in an analogous fashion (**Fig. 3g,** *bottom*). Projections along CD_{choice} remained predictable from uninstructed movements on a single- trial level (**Fig. 3h**; average R^2 across sessions – CD_{choice}: 0.54 ± 0.25; 2 animals, 4 sessions), providing further evidence of the tight link between preparatory dynamics and uninstructed movements.

Uninstructed movements related to behavioral context

We next compared uninstructed movements across task blocks in the two-context paradigm (**Fig. 4**). We found that animals perform qualitatively different uninstructed movements in each behavioral context, despite both contexts requiring instructed movements to the same targets (**Fig. 4a**). Context could be decoded from kinematic features of movement across trial epochs – including during the ITI, in which all external contextual cues are absent (**Fig. 4b,** *top*). The time-course of context decoding from neural population data and from movement kinematics was also similar (**Fig. 4b,** *bottom*).

We sought to understand whether trial-to-trial variability in the neural representation of context-encoding could be predicted from uninstructed movements. We again trained a multiple linear regression model to predict single-trial projections along $CD_{context}$ from kinematic features and found that, like putative choice and urgency dynamics, context-selective signals could be predicted with high fidelity (average R^2 across sessions – **Fig. 4c,d**; $CD_{context}$: $R^2 = 0.49 \pm 0.22$; 6 animals, 12 sessions).

Taken together, these findings suggest that dynamics along CD_{choice}, CD_{ramp}, and $CD_{context}$ could be associated with uninstructed movements and/or the cognitive processes related to the anticipation and planning of upcoming instructed movements and encoding of task context.

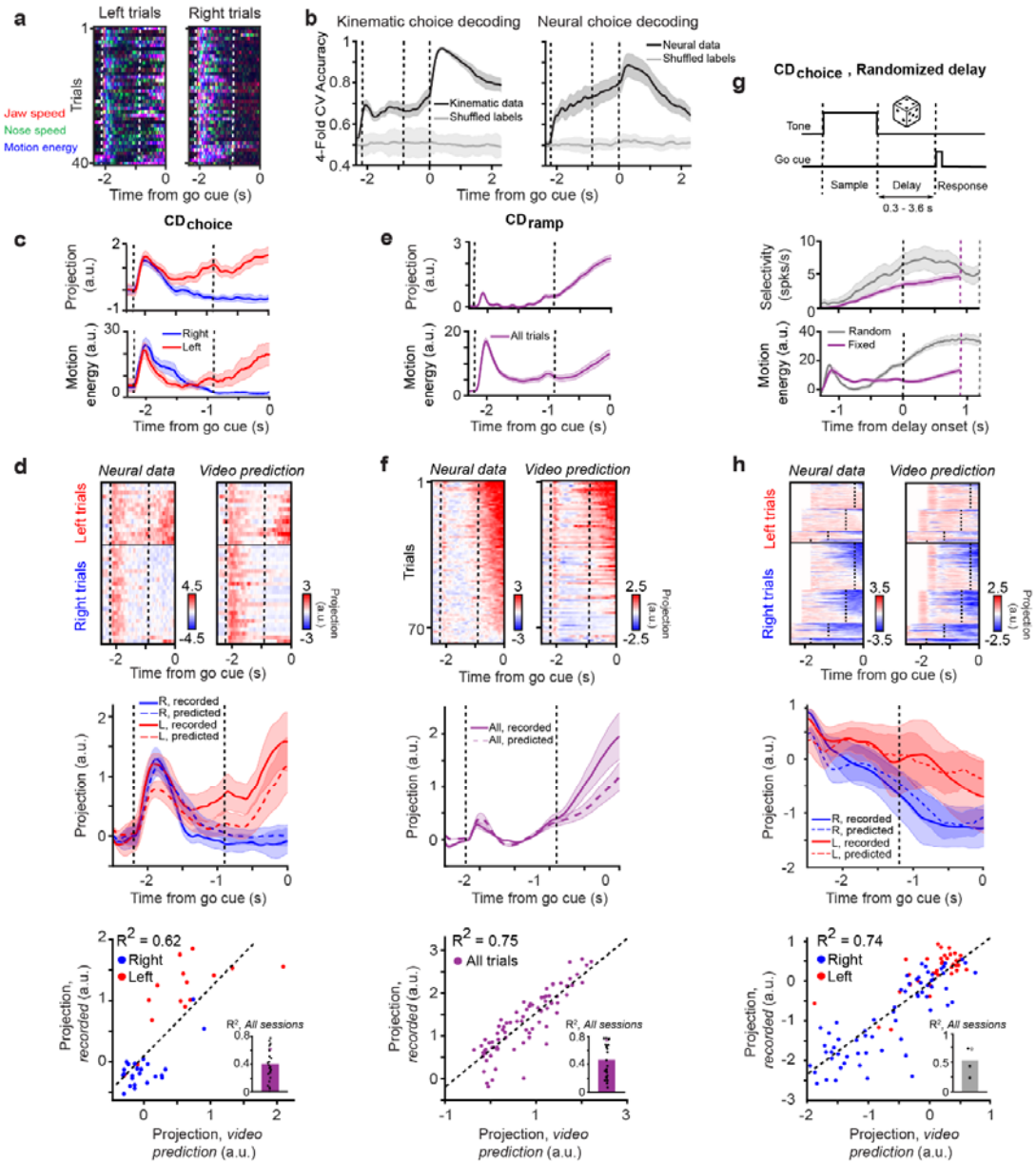

Figure 3 - Uninstructed movements are tightly linked to putative planning dynamics. a. Choice-dependent uninstructed movements. Overlayed trajectories from a random subset of DR trials in an example session. Uninstructed movements are prominent on left, but not right, trials during the delay epoch. **b.** Choice (left vs. right) decoding from kinematic features and neural population data. Gray lines denote shuffled choice labels. Mean and 95% CI of across sessions/shuffles shown. **c.** *Top*, averaged projection onto CD_{choice} on left (*red*) and right (*blue*) trials for the example session depicted in (a). Shaded area, 95% CI across trials. *Bottom*, average motion energy for all correct left and right trials. **d.** Observed and video predictions of single-trial projections of neural activity onto CD_{choice} (see **Methods**) for the same example session as in (a). *Top*, Heatmap of actual and predicted single-trial projections. *Middle*, trial-averaged CD_{choice} projections and predictions. *Bottom*, scatter plot of the average delay epoch projection of neural data onto CD_{choice} versus corresponding video predictions. Dots denote single trials and dashed line denotes linear fit. *Inset*, R^2 values for all sessions (n = 25). Open circle denotes the example session in (a). **e.** Same as (c) but for CD_{ramp} (different example session). Left and right hits are grouped (*purple*). **f.** Same as (d) but for CD_{ramp}. Same session as (e). **g.** *Top*, schematic of the randomized delay task. The delay epoch duration was randomly selected from six values (see **Methods**) with frequencies following an exponential distribution. *Middle*, motion energy averaged across sessions for randomized delay (*gray*) and fixed delay (*purple*) tasks (n = 12 sessions, *randomized delay*; n = 25, *fixed*). *Bottom*, selectivity of all single units pooled across sessions (n = 41 units, *randomized delay*; n = 283, *fixed*). Vertical lines indicate time of delay onset (black), go cue for the fixed delay (*purple*) and or go cue for the randomized delay (*gray*). Only trials with a delay duration of 1.2 s are shown for the randomized delay task for clarity. Shaded areas represent 95% CI in all panels. **h.** Same as (d) for an example session of the randomized delay task. *Top*, trials with delay durations of 0.3, 0.6, 1.2, and 1.8 s are shown. *Middle* and *bottom*, trials with delay duration of 1.2 s only.

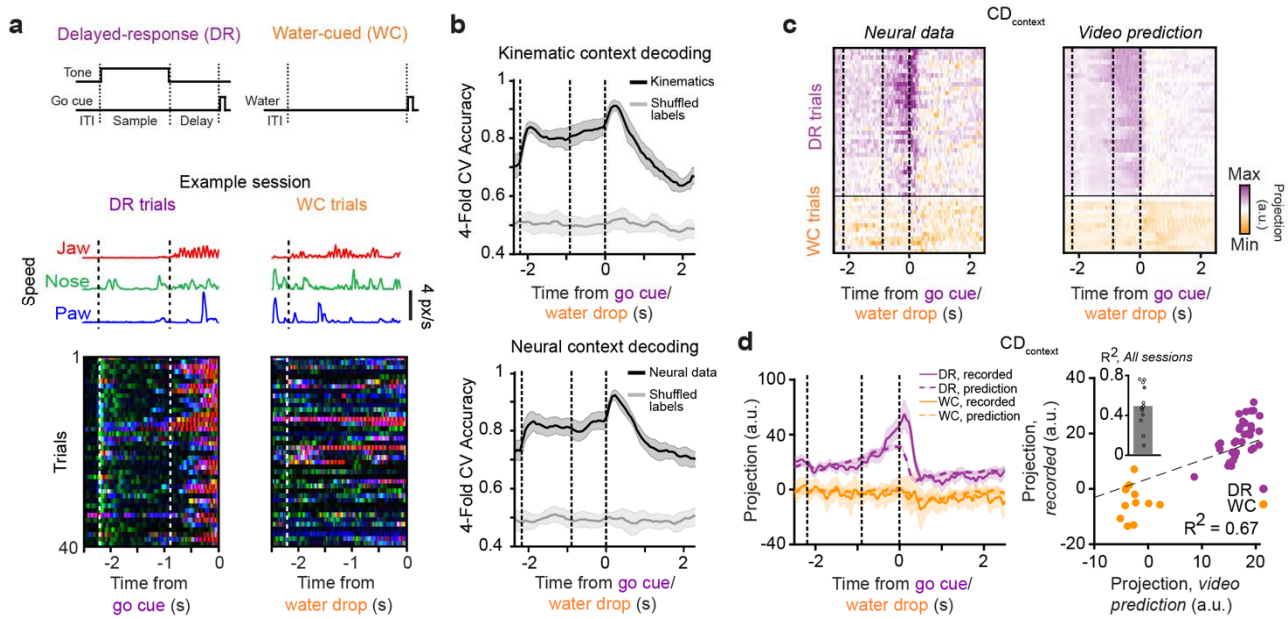

Figure 4 - Uninstructed movements are closely related to the neural encoding of context. a. Schematic of tasks (*top*) and context-dependent uninstructed movements. Jaw/nose/paw movements on an example trial (*middle*) and overlayed trajectories of uninstructed movements across an example session (*bottom*) for DR task (*left*) and WC task (*right*). **b.** Context decoding from high-speed video (*top*) and neural data (*bottom*) as a function of time across all sessions. Gray lines denote shuffled context labels; shaded area, 95% confidence intervals (CI) across sessions. **c.** *Left*, heatmap of single-trial projections of neural data onto $CD_{context}$. *Right*, $CD_{context}$ projections predicted from video in an example session. **d.** *Left*, trial-averaged projection of neural data onto $CD_{context}$ and predictions from video (*dotted lines*) for the example session illustrated in (c). Shaded area, 95% CI across trials. *Right*, scatter plot of average projection of neural data onto $CD_{context}$ during the ITI versus average video prediction. Dots denote single trials; dashed line, line of best fit. *Inset*, R^2 values for all sessions (n = 12). Filled circle denotes the example session in (c).

Subspace decomposition of neural activity

We next examined whether neural signals responsible for the encoding of task variables could be isolated from movement-related signals, despite their correlation in time. We hypothesized that if the neural dynamics associated with cognitive and motor processes are separable, their components in the ALM should be driven by distinct latent signals. Previous theoretical work, later confirmed in primates, suggests that movement planning and execution dynamics can be confined to orthogonal 'null' and 'potent' subspaces of neural activity, respectively[39,40,50]. According to this model, changes in activity along potent dimensions (within the potent subspace) lead to changes in muscle activation, and, thus, movement. Changes along null dimensions (within the null subspace) relate to cognitive processes. We applied this computational framework to determine whether neural dynamics associated with instructed and uninstructed movement could be separated from dynamics associated with the encoding of choice, urgency, and context. Null and potent subspaces were first identified using trial-averaged data from DR and WC trials within each session (see **Fig. 5a** and **Methods**) using procedures described previously[40]. In this formalism, null and potent subspaces are constrained to be orthogonal and are jointly identified with the objective of maximizing the variance explained in the delay epoch (during motor planning) and response epochs (during movement), respectively.

We found that dynamics within null and potent subspaces were confined to the delay and response epochs, respectively, closely resembling results observed in primates (**Fig. 5b-d**). Surprisingly, examining the relationship between activity within the null and potent subspaces and uninstructed movements, we observed that activity within both subspaces was highly correlated with uninstructed movements on single trials (**Fig. 5b,e,f**). One likely explanation for this observation is that decomposing trial-averaged data in this way makes two assumptions that are unlikely to hold. First, this approach assumes that planning- and movement-related processes are strictly

confined to distinct task epochs. Uninstructed movements, however, were expressed across all task epochs (**Figs. 1,3,4**). Second, this approach assumes that cognitive processes and movement do not co-occur in time – for example, that animals did not express uninstructed movements while planning their response or engage cognitive processes during response epoch movements. To address these shortcomings, we sought an analytical approach for identifying null and potent subspaces that avoids these assumptions.

Subspace decomposition of single-trial neural activity

We reasoned that the potent subspace should be defined using single-trial data to account for the trial-to-trial variability in instructed and uninstructed movements. We used motion energy to identify when animals were moving and stationary on a moment-to-moment basis (**see Methods**). Then, null and potent subspaces were identified as the subspaces that maximized variance of neural activity during periods of stationarity and movement, respectively, during all task epochs (**Fig. 5h**). Following this approach for subspace identification, we found that neural dynamics in the potent subspace showed high similarity to motion energy on single trials. Activity in the null subspace was only weakly correlated with movement (**Fig. 5i,l,m**).

Uninstructed movements were commonly observed during the delay epoch of DR trials, during motor planning, and were highly correlated with putative choice and urgency signals (**Fig. 3c-h**). We examined whether the potent subspace inadvertently captured choice or urgency dynamics that are correlated in time with movements. To examine this possibility, we estimated null and potent subspaces using trials from the WC context only. Here, the potent subspace is determined in a context in which choice and urgency signals are absent[23] (**Fig. 2d, EDFig. 3c-f**), precluding the possibility that choice and urgency dynamics are inadvertently captured by the potent subspace. This approach yielded estimates of the null and potent subspaces that were highly similar (**EDFig. 3d-f**). Further, examining null and potent subspaces estimated only using data recorded during the response epoch of both tasks, when planning and urgency dynamics should be minimal, again yielded similar results (**EDFig. 3g-i**). Importantly, these observations suggest that the potent subspace indeed captures movement-related signals, and not separable cognitive signals correlated in time with movements. We also determined whether null and potent subspaces could be better estimated from latent dynamics estimated using factor analysis (FA), Gaussian processes factor analysis[73] (GPFA), and latent factor analysis via dynamical systems[74] (LFADS), but found that these approaches introduced aberrant dynamics (**see Methods**).

We hypothesized that activity in the null and potent subspaces, estimated on single trials, should capture variance in neural activity across all task epochs. Animals may think and move simultaneously; thus, it follows that cognitive dynamics may be present during the response epoch. Additionally, uninstructed movements occur during both the sample and delay epochs, concurrent with stimulus and choice encoding - thus there should be potent dynamics during all task epochs. As expected, activity within null and potent subspaces captured variance across epochs (**Fig. 5k**). Interestingly, the proportion of units with activity largely confined to the potent subspace was much larger than expected by chance (**Fig. 5n** and **EDFig. 4b;** $p=6\text{x}10^{-9;}$ two-sample Kolmogorov-Smirnov test), and much larger than when subspaces were identified from trial-averaged data here (**Fig. 5g**) and in non-human primates[39]. This observation indicates the identification of cellular populations engaged solely in motor processes that could not be identified without properly accounting for uninstructed movements.

Cognitive and motor dynamics during motor planning

The potent subspace may contain three classes of movement-related neural dynamics: (1) motor commands (and efferent copies of motor commands), (2) sensory feedback related to ongoing movements, and (3) cognitive signals that occur *exclusively during periods of movement*. Therefore, we reasoned that if a particular cognitive process was "embodied," in the sense that it is always associated with some externally visible movement, then we would expect to find its associated neural dynamics wholly contained within the potent subspace (**Fig. 6c**). In contrast, cognitive signals driven by processes which are independent of movements should be wholly confined to the null subspace (**Fig. 6a**). Between these extremes, we expect to observe dynamics within both subspaces when a cognitive process influences the expression of uninstructed movements that are driven by distinct latent dynamics (**Fig. 6b**).

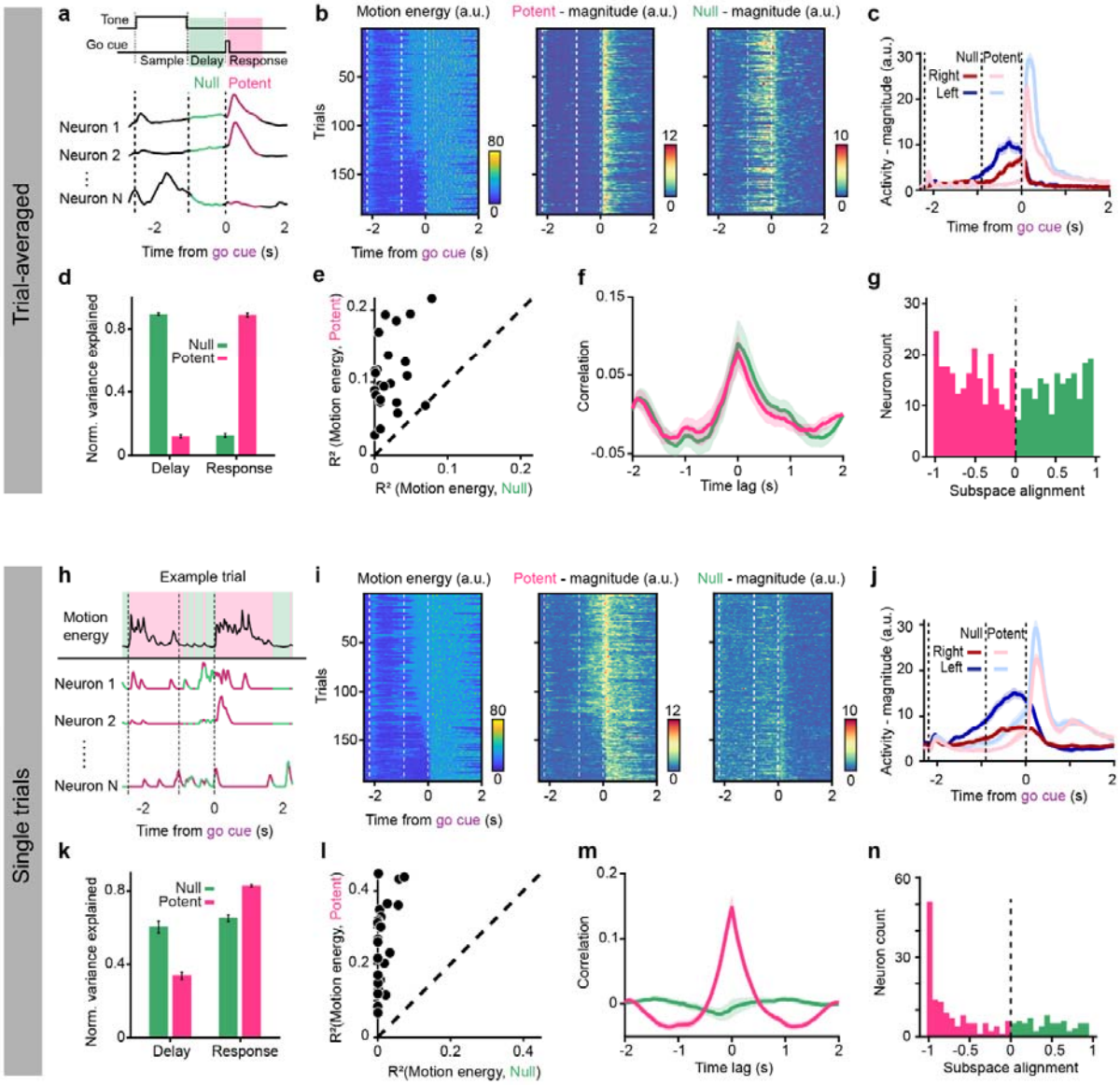

Figure 5 – Subspace decomposition of neural activity using trial-averaged and single-trial data. a. Schematic of the approach for estimating null (*green*) and potent (*pink*) subspaces from trial-averaged neural data. Null and potent subspaces are determined as the orthogonal subspaces that maximally contain the variance of neural activity in the delay and response epochs, respectively. Trials from both DR and WC contexts were used to identify subspaces. **b.** Activity during DR trials within the null and potent subspaces determined from trial-averaged data. *Left*, motion energy across trials. *Middle*, sum squared magnitude of activity in the potent subspace. *Right*, sum squared magnitude of activity in the null subspace. Trials sorted by average delay epoch motion energy. **c.** Sum squared magnitude of activity in null and potent subspaces during DR lick-left and lick-right trials for an example session. Mean and standard error across trials shown. **d.** Normalized variance explained of the neural data during DR and WC trials by the activity in the null and potent subspaces during the delay and response epochs. Null and potent subspaces selectively capture activity in the delay and response epochs, as expected. **e.** Variance explained **(**R^2) of motion energy by the sum squared magnitude of activity in the null and potent subspaces on DR and WC single trials. Each point represents the mean across trials for a session. **f.** Cross-correlation between motion energy and activity in the null and potent subspaces on DR and WC single trials. Mean and 95% CI across sessions shown. **g.** Subspace alignment for all single units across sessions (see **Methods**). Values closer to 1 indicate that more variance of a unit's activity is contained within the null subspace. **h.** Schematic of the approach for estimating null and potent subspaces from single-trial data. Motion energy is used to annotate when an animal is moving (*green*) or stationary (*pink*). These labels are then applied to single-trial neural data. Null and potent subspaces are determined as the orthogonal subspaces that maximally capture the variance of neural activity during periods of quiescence and movement, respectively. Trials from both DR and WC contexts were used to identify subspaces. **i-n.** Same as (b-f**)** but using the single-trial approach for estimating null and potent subspaces.

To evaluate these possibilities, we examined whether putative cognitive signals (illustrated in **Fig. 2**) evolved within the potent and/or null subspaces. We found choice selectivity – dynamics that differentiate left and right DR trials – in both the null and potent subspaces, suggesting that the encoding of choice is separable from dynamics related to the execution of choice-related uninstructed movements. Interestingly, the time course of choice dynamics in

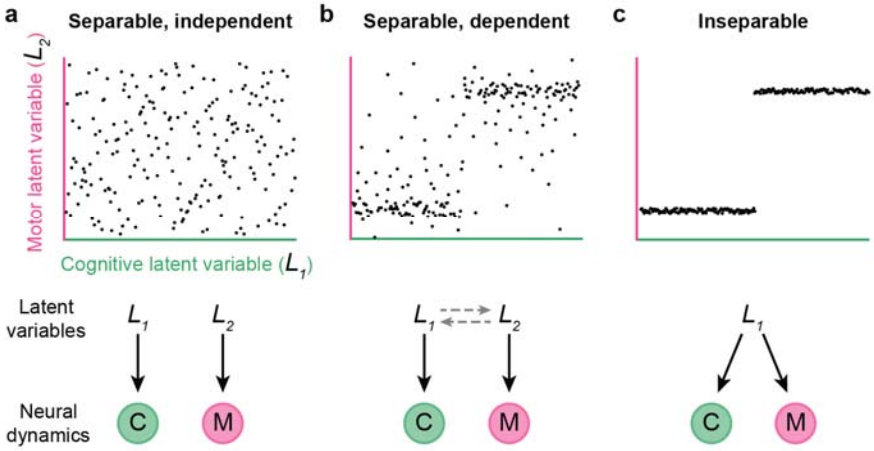

Figure 6 – Schematic of potential relationships between cognitive and movement-related dynamics. a. Some cognitive and movement-related dynamics may be separable and independent from one another. *Top*, toy schematic where a cognitive process and a motor process are each governed by a single latent variable (L_1 and L_2). In this case, the value of the latent cognitive variable (L_1) is independent of the latent motor variable (L_2). *Bottom*, cognitive dynamics, denoted by the green circle, are governed by (black arrow) the latent factor, L_1, while the movement-related dynamics, denoted by the pink circle are governed by a separate, independent latent factor, L_2. **b.** Same as (a) for the separable and dependent case. The value of the latent cognitive variable (L_1) biases (grey dotted arrow) the value of the latent motor variable (L_2). **c.** Same as (b) for the inseparable case. Cognitive and motor dynamics are governed by a single latent variable such that these processes have a nearly one-to-one relationship.

each subspace was distinct, as was their expression on error trials. Selectivity emerged quickly following stimulus presentation in the null subspace and changed little through the delay epoch (**Fig. 7a;** p=0.07; paired t-test comparing selectivity during last 100ms of sample and delay epochs) consistent with a cognitive signal driven by available sensory evidence. On error trials, selectivity in the null subspace initially followed the same trajectory as correct trials but collapsed following stimulus offset. In the potent subspace, in contrast, selectivity continued to increase monotonically during the delay epoch ($p=3\text{x}10^{-13}$; paired t-test comparing selectivity during last 100ms of sample and delay epochs), and no potent subspace selectivity emerged on error trials. These observations suggest that sensory stimuli initially drive appropriate dynamics within the null subspace on error trials, but that choice is not encoded stably and does not engage potent dynamics related to uninstructed movements.

Although the trajectory of choice dynamics in each subspace shared some similarities in trial-averaged data (**Fig. 7a**), they differed markedly on single trials in each subspace. The onset and magnitude of activity along the component of CD_{choice} within the potent subspace tracked trial-type selective motion energy on a moment-by-moment basis (**Fig. 7b, c**). Activity along the component of CD_{choice} in the null subspace tracked choice independently of ongoing uninstructed movements and, importantly, independently of activity within the potent subspace, suggesting that choice-correlated movements are not a result of planning dynamics that 'leak' into the potent subspace. Importantly, we found that many single neurons contribute to either the null or potent subspace representations of CD_{choice}, but not both ($p=1\text{x}10^{-4}$, dip=0.04; Hartigan's dip test of unimodality), providing additional evidence of dynamics that are not only separable, but encoded by distinct populations of neurons (**Fig. 7d**) within the ALM microcircuit.

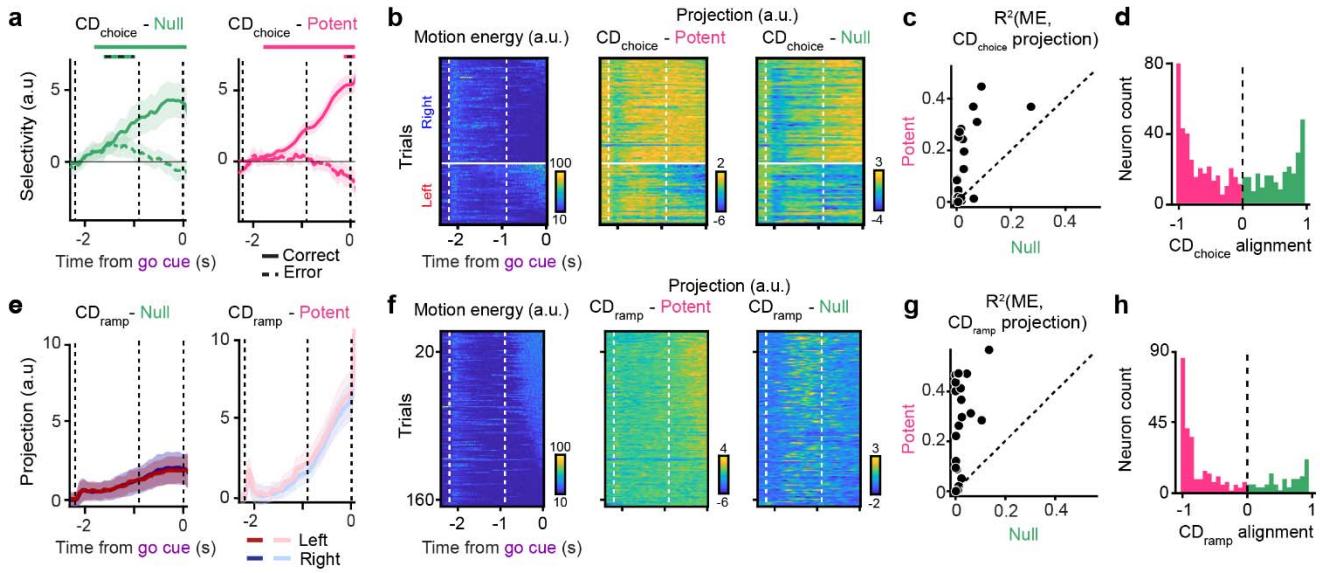

Figure 7 – Subspace decomposition allows for the re-examination of population measures of motor planning. a. Selectivity (neural projections on lick-right trials minus lick-left trials) of null (*left*) and potent (*right*) subspace activity when projected along CD_{choice}. Mean and 5-95% CI of the bootstrap distribution for correct (*solid*) and error (*dashed*) trials shown. Horizontal bars (solid lines, correct trials; solid lines with black dashes, incorrect trials) above plot indicate when the selectivity trace is significantly different from zero ($p<0.05$, one-sided test, bootstrap). **b.** Projections along CD_{choice} in the potent subspace (*middle*), but not the null subspace (*right*), follow the time-course and magnitude of motion energy (*left*) on single lick-left and lick-right trials (example session). **c.** Variance explained **(**R^2) of motion energy by projections along CD_{choice} in the null or potent subspace on single trials. Each point is the average across all trials in a session. **d.** Distribution of single unit alignment with CD_{choice} (see **Methods**). This distribution was significantly different than that expected from a unimodal distribution, indicating the presence of heterogeneous populations contributing to either the null or potent representations of choice ($p=1x10^{-4}$, dip=0.04; Hartigan's dip test of unimodality). **e**. Projection of null (*left*) and potent (*right*) subspace activity along CD_{ramp} on lick-left and lick-right trials. Mean and 95% CI of the bootstrap distribution for correct trials shown. **f-h**. Same as (b-d) for CD_{ramp}. **h.** Distribution of single unit alignment with CD_{ramp}. This distribution was not significantly different than that expected from a unimodal distribution ($p=0.3$, dip=0.02; Hartigan's dip test of unimodality).

Taking a similar approach, we found that ramping dynamics were mostly contained within the potent subspace (**Fig. 7e**) – perhaps surprising given that ramping activity has been interpreted as an urgency or timing signal[69–72]. This observation remained consistent when estimating null and potent subspaces using only WC trials or using only the response epoch of WC and DR trials (**EDFig. 6a, 6d**), when ramping dynamics were not explicitly observed. As a further test of the existence of null-subspace ramping dynamics, we explicitly identified the dimension in the null (and potent) subspace that maximized ramping dynamics – which could be different than the dimension that maximized ramping within the full activity space – and again failed to identify a prominent ramping signal (**EDFig. 6c**). The relative paucity of ramping dynamics in the null subspace suggests that they are not readily separable from associated movements in the ALM (see **Discussion**).

A persistent null-space representation of context.

Next, we examined projections of activity along $CD_{context}$ in each subspace (**Fig. 8a**). We found robust contextual selectivity in both subspaces consistent with the interpretation that both context-correlated movements and a cognitive representation of context and are both encoded within the ALM. The transient, response-epoch dynamics observed along $CD_{context}$ (**Fig 2d,** *far right*) were entirely contained within the potent subspace (**Fig. 8a**) likely indicative of subtle context-specific differences in instructed movements. We then compared context selectivity (the difference in projections onto $CD_{context}$ on DR vs. WC trials) on trials with high motion energy during the ITI ('Move' trials) and trials with minimal ITI motion energy ('Quiet' trials). Context selectivity within the null

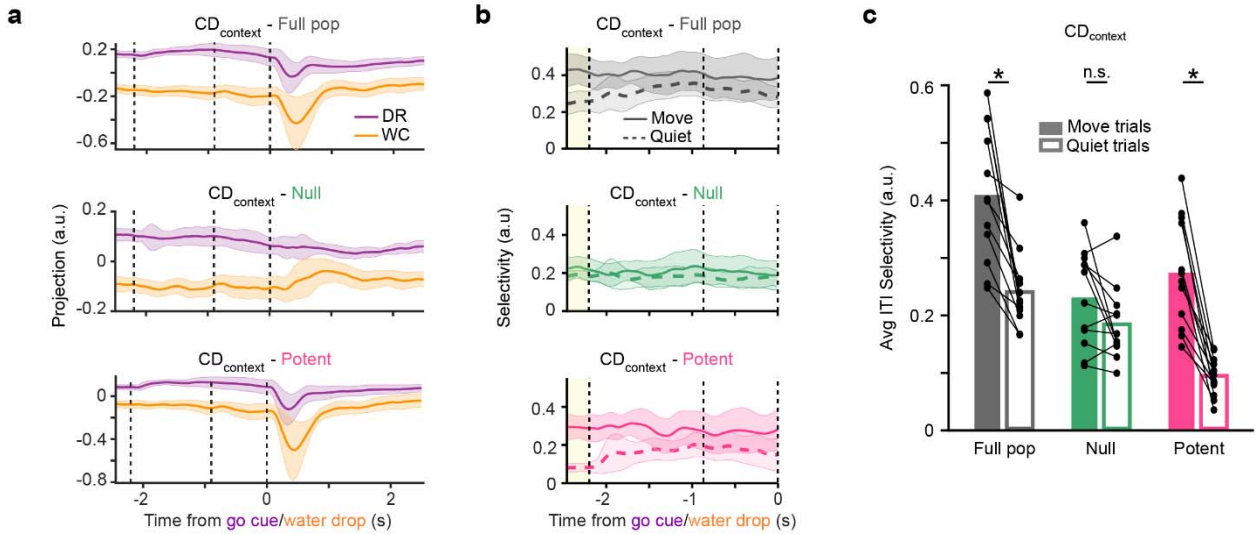

Figure 8 – A persistent, cognitive representation of context in the null subspace. a. Projections along $CD_{context}$ found using all neural activity (*top*), activity in the null subspace (*middle*), or the potent subspace (*bottom*). Solid lines denote the mean projection across sessions (n = 12) for DR hits (*purple*) and WC hits (*orange*); shaded area, 95% CI across sessions. Transient response epoch dynamics are absent in the null subspace. **b.** Selectivity in $CD_{context}$ projections (DR – WC trials) on 'move' (*solid lines*) or 'quiet' (*dashed*) trials. Lines denote the mean selectivity across sessions (n = 12) in the full space of neural activity (*top*), activity within the null subspace (*middle*), and potent subspace (*bottom*); shaded area, 95% CI across sessions. Yellow region denotes ITI used to define 'move' and 'quiet' trials. **c.** Average $CD_{context}$ selectivity during the ITI (yellow shaded region in *(b)*) for 'move' (*filled bars*) vs. 'quiet' (*open bars*) trials. Dots denote single sessions; bars, mean across sessions. Asterisks denote significant differences ($p < 0.01$) in $CD_{context}$ selectivity between 'move' and 'quiet' trials (*p*-values from left to right, Full population: $p = 0.005$, Null: $p = 0.5$, Potent: $p = 2\text{x}10^{-4}$; *paired t-test*).

subspace was indistinguishable in high- and low-movement trials. In contrast, context selectivity within the potent subspace was considerably larger on 'Move' trials, demonstrating that a null – but not a potent – representation of context persists in the absence of movement (**Figs. 8b,c**; Selectivity on 'Move' vs. 'Quiet' trials – Full population: $p = 0.005$, Null: $p = 0.5$, Potent: $p = 2\text{ x}10^{-4}$; paired *t*-test). These observations suggest that the analysis of context-dependent dynamics without subspace decomposition indeed spuriously conflated separate latent dynamics responsible for a cognitive representation of context (contained within the null subspace) and related to context-dependent movements (contained in the potent subspace). Decomposing neural activity into null and potent subspaces enables the identification of separable motor and cognitive components of contextual encoding.

Encoding of tongue kinematics in the potent subspace

Finally, we asked whether trial-type dependent activity following the go cue relates to movement, according to previous suppositions[58,63] (**EDFig. 7**). Left-right selectivity along CD_{action} existed within both the null and potent subspaces (**EDFig. 7a**), although the magnitude of selectivity in the null subspace was less than that within potent subspace. On error trials, the activity along CD_{action} flipped to resemble that of the other trial type in the null subspace but flipped asymmetrically within the potent subspace. This asymmetry closely corresponded to an asymmetry in tongue angle, with incorrect movements directed to less extreme angles when directed to the left, on average (**EDFig. 7b,c**). The component of CD_{action} within the potent subspace also better tracked moment-to-moment changes in tongue angle during the response epoch (p=2 x10^{-8}; paired *t*-test) (**EDFig. 7d,e**). The similarity between tongue angle and dynamics along CD_{action} again suggests that neural dynamics in the potent subspace relate to movement kinematics. The interpretation of action dynamics within the null subspace remains unclear but could relate to the motor plan for directional licking.

<u>Discussion</u>

We aimed to understand whether the neural correlates of three cognitive variables commonly examined in sensorimotor decision-making tasks – choice, urgency, and context – were separable from the neural encoding of related uninstructed movements in the mouse ALM. We addressed this question by adapting an analytical formalism in which neural activity is decomposed into orthogonal subspaces – a movement-potent subspace containing dynamics related to the execution of movements and a complementary movement-null subspace containing dynamics related to cognitive processes[39,40,50]. Extending upon this framework allowed us to consider single-trial neural data recorded in the presence of uninstructed movements that can vary dramatically across trials in their timing and identity (**Fig. 5**).

Separability of choice, urgency, and context encoding from movement-dynamics

Using this approach, we demonstrated that the ALM contains neural dynamics related to encoding of choice and context that could be readily separated from movements, despite both cognitive variables being strongly correlated with movements in time (**Fig. 7** and **Fig. 8**). Choice-selective signals were present in both null and potent subspaces (**Fig. 7a**), consistent with the interpretation that a cognitive representation of choice within the null subspace biases the probability and identity of uninstructed movements in a choice-selective manner. Supporting this interpretation, null and potent subspace dynamics followed similar trajectories on average but differed markedly at the single-trial level (**Fig. 7b**). Further, null subspace encoding of choice exhibited features absent from encoding within the potent subspace. Choice encoding strengthened only with the availability of sensory evidence, while potent subspace encoding continued to increase monotonically after sensory stimuli were removed, mirroring the temporal evolution of animal's uninstructed movements. On error trials, stimulus-driven choice encoding initially evolved correctly – but only within the null subspace – before decaying prior to the go cue (**Fig. 7a**). Together, these results suggest cognitive and motor processes that are governed by separable latent processes (**Fig. 6b**).

Context was stably encoded within the null subspace during all trial epochs and the inter-trial interval (**Fig. 8a-c**). Although context was strongly represented in the potent subspace as well, these dynamics were abolished in the absence of movement and were modulated by animals' instructed movements. These results suggest a persistent cognitive encoding of context in the null subspace, and distinct potent-subspace dynamics related to context-dependent movements, again indicative of related, but separable, latent processes (**Fig. 6b**).

Surprisingly, trial-averaged ramping dynamics proposed to underlie urgency (or timing)[69–72] were principally represented in the potent subspace (**Fig. 7e**) indicating the possible absence of a cognitive representation of urgency that can be dissociated from movements in the ALM. Although it remains possible that one exists in another brain region, our results suggest the embodiment of urgency in our behavioral paradigm[75,76].

In contrast to these cognitive variables, encoding of kinematic features of movements, which were not used to determine subspaces, was confined to the potent subspace (**EDFig. 7**)

Subspace decomposition

The approach to subspace decomposition presented here represents a means for assessing the issue of separability, and for isolating separable dynamics into motor- and non-motor components for further analyses across a wide range of experimental preparations. This method only requires annotation of when animals are moving and utilizes a robust analytical approach not sensitive to parameter tuning.

A number of alternative methods have been proposed to evaluate neural dynamics associated with cognitive processes in the presence of movement. The most common approach, which assumes separability of cognitive and motor dynamics, is to parameterize movements as fully as possible and 'regress them out.' However, parameterization of movement, particularly the orofacial and postural movements that have been associated with strong, brain-wide neural dynamics[5,30,31], can be challenging. Further, this approach typically assumes a linear relationship between neural activity and kinematic (or electromyographic) variables – an assumption unlikely to hold for common movements mediated by central pattern generators and other highly nonlinear mechanisms[77–79]. Subspace decomposition is straightforward to implement under a range of experimental conditions and does not preclude complex, nonlinear relationships between neural activity and movement variables, as expected for many

orofacial movements[77]. Methods for properly interpreting cognitive signals in the presence of related movements on single trials will be vital for increasingly common experimental paradigms examining freely moving animals performing complex, naturalistic behaviors[80–90].

Determination of null and potent subspaces as the orthogonal subspaces containing the most variance in neural activity during periods of stationarity and movement is conservative in the assignment of dynamics to the null subspace. It is more likely that cognitive dynamics are misassigned to the potent subspace than movement-related dynamics to the null subspace. For example, dynamics associated with "embodied" cognitive processes that always occur during periods of movement will only be represented in the potent subspace. Thus, the existence of dynamics within the null subspace are highly likely to indicate cognitive signals. Nevertheless, we found that the potent subspace captures similar dynamics when estimated from data recorded during the response epoch ('instructed' movements) or from WC trials, where uninstructed movements occur in the absence of choice and urgency signals (**EDFig. 3, 6a,d**). This observation argues against the possibility that additional cognitive dynamics associated with choice and urgency were inadvertently assigned to the potent subspace due to their correlation in time with uninstructed movements.

That many individual neurons contribute solely to one subspace (**Fig. 5n, 6d,h**) suggests that the complementary subspaces we identify map to distinct cell types within the underlying cortical circuit[62,91]. This observation that individual neurons only appear to code for either cognitive or motor variables when uninstructed movements are accounted for (**Fig. 5n, 6d,h**) underscores the importance of properly considering movements in future work focused on the roles of anatomically- or transcriptomically-defined cell-types in neural computation.

Our approach to subspace decomposition makes several simplifying assumptions. First, movements of the posterior torso, hindlimbs, or tail of the animal were not captured via videography. It remains possible, albeit unlikely, that animals commonly perform movements confined to these portions of the body without concomitant movement of the forepaws, head, neck, face, or whiskers[26]. Periods of stationarity were no doubt algorithmically classified imperfectly and could have contained subtle movements below our threshold for detection. Second, we did not consider potential time lags between motion energy captured via videography and the dynamics associated with motor and/or sensory signals[92]. However, these time lags, on the order of a few tens of milliseconds, should be much shorter than the timescale of dynamics explored in this study. Third, the set of signals related to movement and/or cognitive processes may also be better described as occupying nonlinear manifolds rather than linear subspaces[93,94]. Subspaces (or manifolds) could also shift dynamically during behavior following changes in the activation of upstream or downstream brain regions[95,96] or changes in context[16,48,97]. Considering this additional complexity may improve estimates of the dynamics associated with specific neural processes.

Variable relationships between cognition and movement

The dynamics associated with some movements and cognitive processes may be largely independent (**Fig. 6a**) – perhaps in the case of the locomotor patterns of an individual thinking about where they might spend an upcoming holiday while walking down the street. On the other hand, some cognitive processes may be embodied, in the sense that they are tightly linked to externally observable changes in the body (**Fig. 6c**), such as the relationship between arousal and changes in pupil diameter[98–100]. Between these extremes may be movements which are correlated with, but separable from, cognitive processes. The probability and identity of uninstructed movements in this study appeared related to choice and context (**Fig. 6b**), but with a high degree of trial-to-trial and moment-to-moment variability unlikely to reflect commensurate variability in the cognitive processes to which they relate. Correlations between cognitive processes and movements may also differ considerably in highly trained, head-fixed animals compared to naturalistic settings[83,88]. This high degree of variability in these relationships underscores the importance of developing and utilizing tools for assessing whether the neural activity supporting cognitive processes can be dissociated from those related to movements in particular experimental paradigms of interest.

The tight link between cognition and movement might suggest that some cognition-associated movements may be beneficial for behavior. For example, postural adjustments may be highly related to decisions or motor plans, enabling faster reaction times and/or more accurate movements[5,33]. Movements are also essential for some

cognitive processes – those supporting active sensation of the environment surely facilitate the construction and continual updating of internal models of the environment[30,46]. However, just as separability may not be consistent across movements and cognitive processes, not all cognition-associated movements may have a functional role[30,101]. A poker player's 'tell' may be highly related to their cognitive state, yet may not directly aid the player in the game. Regardless of their functional relationship, understanding the separability of cognitive processes and associated movements in a wide variety of experimental settings will be essential for the interpretation of neural dynamics observed during behavior.

Methods

Animals

This study used data collected from 13 mice; both male and female animals older than 8 weeks were used. Six animals were used for the two-context task and were either C57BL/6J (JAX 000664) or VGAT-ChR2-EYFP (-/-) (bred in-house). An additional three animals, either C57BL/6J or VGAT-ChR2-EYFP (-/-) were trained only on the delayed response task. A separate cohort of two animals were used in the randomized delay task (VGAT-ChR2-EYFP (+/-). Finally, two VGAT-ChR2-EYFP (+/-) animals were used in optogenetics experiments. Mice were housed in a 12-hour reverse dark/light cycle room with ad libitum access to food. Access to water was restricted during behavioral and electrophysiology experiments, for details see section ***Mouse behavior.*** Sample sizes for all experiments were determined based on what is standard in the field; sample sizes were not determined using any statistical tests.

Surgical procedures

All performed surgical procedures were in accordance with protocols approved by Boston University Institutional Animal Care and Use Committee. For post-operative analgesia, mice were given ketaprofen (0.1 mL of 1 mg/mL solution) and buprenorphine (0.07 mL of 0.03 mg/mL solution) prior to the start of all surgical procedures. Mice were anesthetized with 1-2% isoflurane and placed on a heating pad in a stereotaxic apparatus. Artificial tears (Akorn Sodium Chloride 5% Opthalamic Ointment) were applied to their eyes and a local anesthetic was injected under the skin (Bupivacaine; 0.1 mL of 5 mg/mL solution) above the skull. The skin overlying the skull was removed to expose the ALM (AP: +2.5 mm, ML: +1.5 mm), bregma, and lambda. The periosteum was removed and the skin was secured to the skull with cyanoacrylate (Krazy Glue) around the margins. For electrophysiology experiments, a headbar was implanted just posterior to bregma and secured with superglue and dental cement (Jet™). Wells to hold cortex buffer during electrophysiology recordings were sculpted using dental cement and a thin layer of superglue was applied over any exposed bone.

For optogenetics experiments, after headbar implantation, bone overlying frontal cortex was thinned bilaterally with a dental drill and removed, exposing the frontal cortex. A glass window was then implanted over each hemisphere and secured to the skull with cyanoacrylate[102]. Before performing photoinactivation experiments, any bone regrowth was removed.

Mouse behavior

Following surgery, mice were allowed to recover for ~1 week and then water restricted, receiving 1.0 mL of water per day. Behavioral training commenced after animals had been water restricted for 3-4 days. If animals received less than 1.0 mL during training, they were supplemented with additional water.

All mice used in experiments were first trained on the delayed-response task with a fixed delay epoch until they reached at least 70% accuracy. At the beginning of each trial, one of two auditory tones lasting 1.3 s were played; the tone indicating a 'right' trial was white noise while the tone indicating a 'left' trial was a pure tone (8 kHz). The delay epoch (0.9 s for 12 mice, 0.7 s for 1 mouse and linearly time warped to 0.9 s) started after the completion of the sample tone. Following the delay epoch, an auditory go cue was played (swept-frequency cosine [chirp], 10 ms) after which animals were rewarded with ~3 µL of water for contacting the correct lickport. Lickport contacts before the response epoch resulted in the current task epoch restarting, ensuring that they could not progress to the next task epoch until they had stopped licking for the specified length of the current epoch. If

the animal did not respond within 3 s of the go cue, this was considered an 'ignore' trial, although responses were typically registered within 300 ms of the go cue.

Mice used for the two-context task *(***Figs. 1,2,4,8** and **EDFig. 1-3***)* were introduced to the water-cued context after they were fully trained on the delayed-response context and at least two days before the first electrophysiology recording session. A behavioral session began with ~100 DR trials and was then followed with interleaved blocks of WC and DR trials. Each interleaved block was 10-25 trials, with no fixed block duration. All sessions started with DR trials because sessions that began with WC trials had to be terminated early due to a high 'no response' rate, likely due to the mouse becoming sated early in the session (*data not shown*). In a WC trial, all auditory cues were omitted and a ~3 µL water reward was presented randomly from either lickport. Trials in which the animal contacted the lickport prior to the reward ('early lick') were omitted. Inter-trial intervals were randomly drawn from an exponential distribution with mean 1.5 s. There were no explicit cues during the ITI to indicate to the animal which context block it was in.

For the randomized delay task *(***Fig. 3g-h***)*, mice were first fully trained on the fixed delay DR task (delay duration of 0.9 s). The delay epoch length was then randomized – the duration was randomly selected from six possible values (0.3, 0.6, 1.2, 1.8, 2.4, and 3.6 s). The probability of each delay duration being selected was assigned such that it resembled a cumulative distribution function of an exponential distribution with $\tau = 0.9$ s, as in ref [64]. Animals were trained on this version of the task until they became experts (> 70% accuracy and < 20% early lick rate).

Videography analysis

High-speed video was captured (400 Hz frame rate) from two cameras (FLIR, Blackfly® monochrome camera, Model number: BFS-U3-16S2M-CS). One provided a side view of the mouse and the other provided a bottom view. We tracked the movements of specific body features using DeepLabCut[52] (**Figs. 1,3,4**). The tongue, jaw, and nose were tracked using both cameras while the paws were only tracked using the bottom view. Position and velocity of each tracked feature was calculated from each camera. The x and y position of each kinematic feature was extracted from the output of DeepLabCut. Missing values were filled in with the nearest available value for all features except for the tongue. The velocity of each feature was then calculated as the first-order derivative of the position vector. Tongue angle and length were found using the bottom camera. Tongue angle was defined as the angle between the vector pointing from the jaw to the tip of the tongue and the vector defining the direction the mouse was facing. Tongue length was calculated as the Euclidean distance from the jaw to the tip of the tongue.

Plots of kinematic feature overlays (**Fig. 1e, 3a, 4a and EDFig. 2**) were generated by plotting an [r, g, b] value for each timepoint, *t*, where the values were specified by [KinFeature1_t, KinFeature2_t, KinFeature3_t]. All kinematic features (speed or motion energy) were first standardized by taking the 99th percentile across time and trials and normalizing to this value.

Motion energy

The motion energy for a given frame and pixel was defined as the absolute value of the difference between the median value of the pixel across the next 5 frames (12.5 ms) and the median value of the pixel across the previous 5 frames (12.5 ms). Motion energy for each frame was then converted to a single value by taking the 99th percentile across pixels. A threshold above which an animal was classed as moving, below which stationary, was defined on a per session basis and set using a manual approach. Motion energy distributions, per session, were bimodal, showing a large peak with little variance at low motion energy values and a second, smaller peak, with high variance at large values. The threshold was set as the motion energy value separating these two mixtures. We found that this method of setting the threshold captured both short and long duration movements. Alternative methods such as defining baseline period of movements with which to compare against were less successful due to the variability in timing of the movements across trials.

Photoinactivation experiments

Optogenetic photoinactivation was deployed on ~30% of trials selected at random. A 'masking flash' (470 mm LED's LUXEON REBEL LED) controlled by an Arduino Teensy microcontroller (100 ms pulses, at 10 Hz) was delivered constantly for the duration of the session to prevent mice from differentiating control and photoinactivation trials. A 488 nm laser (Coherent OBIS 488 nm LX 150 mW Laser System) was used for all photoinactivation experiments. ChR2-assisted photoinactivation (**Fig. 1b,c,g-i; EDFig. 1b-d**) was performed through a cranial window[102] (see ***Surgical Procedures***), which replaced bone over the frontal cortex. Light was delivered either at the start of the delay epoch, or at the start of the response epoch per session. A power density of 1.5 mW/mm^2 was used for all photoinactivation experiments.

For delay epoch photoinactivation (**Fig. 1g-i; EDFig. 1b**), light was delivered at the onset of the delay epoch and lasted for 0.6 s followed by a 0.2 s ramp down. We targeted one of three regions per session: bilateral motor cortex, bilateral ALM, or bilateral tjM1. A scanning galvo system (THORLABS GPS011) was used to simultaneously target both hemispheres by scanning at 40 Hz. The beam (2 mm diameter) was centered around the following locations: ALM (AP 2.5 mm, ML 1.5 mm), tjM1 (AP 1.75 mm, ML 2.25 mm), motor cortex (i.e. ALM and tjM1; AP 2.25 mm, ML 1.85 mm). Due to their proximity, when specifically targeting ALM or tjM1, Kwik-Cast™ (World Precision Instruments) was applied to the surrounding regions to prevent photoinactivation of other regions.
For photoinactivation at the go cue (**Fig. 1b,c; EDFig. 1c,d**), light was delivered to the motor cortex for 0.8 s followed by a 0.2 s ramp down beginning at the go cue presentation.

Electrophysiology recordings
Extracellular recordings were performed in the ALM using one of two types of silicon probes: H2 probes, which have two shanks, each with 32 channels with 25 µm spacing (Cambridge Neurotech) or Neuropixels 1.0[103] which have one shank and allow recording from 384 channels arranged in a checkerboard pattern (IMEC). For recordings with H2 probes, the 64-channel voltage signals were multiplexed using a Whisper recording system (Neural Circuits, LLC), recorded on a PXI-8133 board (National Instruments) and digitized at 14 bits. The signals were demultiplexed into 64 voltage traces sampled at 25 kHz and stored for offline analysis.

At least 6 hours before recording, a small craniotomy (1-1.5 mm diameter) was made over ALM (AP 2.5 mm, ML 1.5 mm). 2-5 recordings were performed on a single craniotomy on consecutive days. After inserting the probes between 900 and 1100 µm (MPM System, New Scale Technologies), brain tissue was allowed to settle for at least 5 minutes before starting recordings. All recordings were made using SpikeGLX (https://github.com/billkarsh/SpikeGLX).

Behavioral analysis
All sessions used for behavioral analysis had at least 40 correct DR trials for each direction (left or right) and 20 correct WC trials for each direction, excluding early lick and ignore trials, which were omitted from all analyses. To assess the impact of ALM photoinactivation at the go cue, we first calculated the percent of trials with a correct lick within 600 ms of the go cue (**Fig. 1c**). To find the fraction of time with the tongue visible during the photoinactivation period (**EDFig. 1d**), for each trial we found the number of time-points within the 1 s after the go cue where the tongue was labelled as visible by DeepLabCut and divided that by the total number of time-points within the photoinactivation period. This was then averaged for all control or photoinactivation trials for a given session.

To assess the impact of bilateral MC/ALM/tjM1 photoinactivation during the delay epoch, the average motion energy during the delay epoch was calculated separately for right and left control vs. photoinactivation trials (**Fig. 1h, EDFig. 1b**).

Electrophysiology recording analysis
JRCLUST[104] (https://github.com/JaneliaSciComp/JRCLUST) and/or Kilosort3 (https://github.com/MouseLand/Kilosort) with manual curation using Phy (https://github.com/cortex-lab/phy) were used for spike sorting. For the DR task we recorded 1651 units (483 single units) in ALM from 25 sessions using 9 mice. 12 of these sessions in 6 of the mice were utilized for the analyses of the two-context task. 522 units (214 well-isolated single units) were recorded in these sessions. Finally for the randomized delay task we

recorded 226 units (41 well-isolated single units) in ALM from 4 sessions using 2 mice. All units were included in analyses with the exceptions of subspace alignment (**Fig. 5g,n** and **Fig. 7d,h**) and single-unit selectivity analyses (**Fig. 3g** and **EDFig. 3c**) where only well-isolated units were included.

To find choice-selective neurons (**Fig. 2**), forty trials were subsampled for both right and left correct trials and a *ranksum* test was used to compare spike counts for each unit during the sample, delay, or response epochs. Selective units were those with significantly different spike counts ($p < 0.05$, ranksum test). Context selective units (**Fig. 2**) were defined in the same manner but comparing spike counts during the ITI (the 300 ms preceding the sample tone onset).

Selectivity in the neural population (**Fig. 3g, EDFig. 3c**) was calculated as the difference in spike rate on *preferred – non-preferred* trials in choice-selective units, with *preferred* trials referring to the trial type with a higher spike rate for each unit.

<u>*Coding direction analysis*</u>

Coding directions (CD) were defined as directions in neural activity state space, defined by trial-averaged data, that maximally separated trajectories of two conditions. Trial-averaged neural activity for each condition c was formatted in a matrix $\mathbf{X}_c \in \square^{T \times N}$, where T is the number of time bins and N the number of units. Each $\mathbf{X}_c$ was baseline subtracted and scaled by baseline standard deviation before estimating CDs.

CD_{choice} and CD_{action} were calculated as:

$$\boldsymbol{v} = \frac{\overline{\boldsymbol{x}}_{lickright} - \overline{\boldsymbol{x}}_{lickleft}}{\sqrt{\mathrm{var}(\overline{\boldsymbol{x}}_{lickright}) + \mathrm{var}(\overline{\boldsymbol{x}}_{lickleft})}}$$

$$\boldsymbol{CD} = \frac{\boldsymbol{v}}{\sum |\boldsymbol{v}|}$$

For each unit, the mean spike rate difference between right lick trials, $\overline{\boldsymbol{x}}_{lickright}$, and left lick trials, $\overline{\boldsymbol{x}}_{lickleft}$, was calculated in a 400 ms time interval. CD_{choice} was calculated in the last 400 ms of the delay epoch and CD_{action} was calculated in the first 400 ms of the response epoch. The vector $\boldsymbol{v}$ was then obtained by normalizing by the square root of the sum of the variances across conditions. Finally, $\boldsymbol{v}$ was normalized by its L_1 norm to ensure projections do not scale by the length of $\boldsymbol{v}$, the number of units simultaneously recorded.

CD_{ramp} was calculated as:

$$\boldsymbol{v} = \frac{\overline{\boldsymbol{x}}_{delay} - \overline{\boldsymbol{x}}_{ITI}}{\sqrt{\mathrm{var}(\overline{\boldsymbol{x}}_{delay}) + \mathrm{var}(\overline{\boldsymbol{x}}_{ITI})}}$$

$$\boldsymbol{CD} = \frac{\boldsymbol{v}}{\sum |\boldsymbol{v}|}$$

This calculation was similar to the calculations of CD_{choice} and CD_{action} but incorporated data from all correct DR trials during the last 400 ms of the delay epoch, $\overline{\boldsymbol{x}}_{delay}$, and during the ITI (300 ms preceding the sample tone onset), $\overline{\boldsymbol{x}}_{ITI}$.

$CD_{context}$ was calculated as:

$$\boldsymbol{v} = \frac{\overline{\boldsymbol{x}}_{DR} - \overline{\boldsymbol{x}}_{WC}}{\sqrt{\mathrm{var}(\overline{\boldsymbol{x}}_{DR}) + \mathrm{var}(\overline{\boldsymbol{x}}_{WC})}}$$

$$\boldsymbol{CD} = \frac{\boldsymbol{v}}{\sum |\boldsymbol{v}|}$$

This calculation was similar to the calculation of other CDs but incorporated data from correct DR, $\overline{\boldsymbol{x}}_{DR}$, and WC, $\overline{\boldsymbol{x}}_{WC}$, trials during the ITI.

CD_{action} was orthogonalized to CD_{choice} to exclusively capture response epoch selectivity that emerges after the go cue. CD_{ramp} was orthogonalized to CD_{action} and CD_{choice} to remove selectivity that may emerge during the response epoch that is also captured in CD_{action}. Orthogonalization was performed using the Gram-Schmidt process.

Projections of the population activity along the CD were calculated as:

$$proj = \boldsymbol{CD}^T * \overline{\boldsymbol{x}}$$

For the randomized delay task, trials with non-1.2 s delay lengths were used to calculate CD_{choice} (fit trials), always using the last 600 ms of the delay epoch as the time interval for calculation[64]. Population activity from trials with 1.2 s delays (test trials) were then projected along the CD_{choice} (**Figure 3h - *middle***). For visualization purposes, trials with all delay lengths (including fit trials) were projected along CD_{choice} in **Figure 3h – *top*.**

Choice/context decoding from neural population or kinematic features

We trained logistic regression models to predict either animal choice (**Fig. 3b**) or behavioral context (**Fig. 4b**) from either kinematic features or single trial neural activity. The kinematic regressors were made up of the x and y positions and velocities of DLC tracked features (tongue, jaw, and nose), as well as the tongue length, angle, and motion energy. The neural regressors were the firing rates of the units simultaneously recorded within each session. Animal choice was encoded as -1 on right lick trials and 1 on left lick trials. Context was encoded as 1 on DR trials and -1 on WC trials. Both correct and error trials were used for this analysis. A separate model was trained at each time bin for both neural and kinematic decoding. Models were trained with ridge regularization and 4-fold cross-validation with 30% of trials held out for testing. Chance accuracy was obtained by shuffling choice/context labels across trials. Accuracy of the prediction was defined as:

$$Accuracy = \frac{Number\ of\ correct\ predictions}{Total\ number\ of\ predictions}$$

Predicting projections along coding directions from kinematic features

We trained support vector machines (SVM) to predict projections along CD_{choice}, CD_{ramp}, and $CD_{context}$. Correct DR trials were used for predicting CD_{choice} and CD_{ramp} projections; correct DR and WC trials were used for predicting $CD_{context}$. For predicting $CD_{context}$, the regressors were made up of the x and y positions and velocities of DLC tracked features (tongue, jaw, and nose), as well as the tongue length, angle, and motion energy (totaling 60 regressors). Only the sample and delay epoch were considered when predicting CD_{choice} and CD_{ramp} projections; because of this, any tongue-related metrics were not included as regressors in these analyses (totaling 55 regressors). Projections and kinematic features were first mean-centered and scaled to unit variance before input to the regression model. The previous B bins of kinematic data were used to predict the current bin's neural data (B=6, each bin is 5 ms). Models were trained with ridge regularization and 4-fold cross-validation, however similar results were obtained with unregularized regression. The models were tested on held-out testing data (40% of trials for CD_{choice} and CD_{ramp}; tested on 30% of trials for $CD_{context}$). To assess the prediction quality between projections and model predictions, we calculated the variance explained as:

$$R^2 = 1 - \frac{\sum_t (y_t - \hat{y}_t)^2}{\sum_t (y_t - \overline{y})^2}$$

where y_i is the value of the projection at time t, $\hat{y}_t$ is the prediction, and □ is the mean of the projection across all time.

When predicting projections along CD_{choice} during the randomized delay task, unregularized models were used (**Fig. 3h**). This was due to the small numbers of trials for each delay length which precluded the partitioning of data into 3 separate sets (training, validation, and testing trials). Instead, models were trained with linear regression and 4-fold cross-validation and tested on held-out data from each cross-validation fold. For assessing prediction quality between projections and model predictions, trials with 1.2 s delay epochs were used.

To understand which groups of kinematic features were most informative for predicting projections along CD_{choice}, or $CD_{context}$ (**EDFig. 2**), the absolute value of the beta coefficients for each kinematic regressor in the trained model was first obtained. For each feature group (jaw, nose, motion energy), the average beta coefficient across all regressors belonging to this kinematic feature group (*8*nBins* for jaw, *6*nBins* for nose, and *1*nBins* for motion energy) was calculated. The average beta coefficient for each feature group was then expressed as a fraction of the total of all beta coefficients.

Subspace identification

Null and potent subspaces were identified following the general approach described in ref[40]. For identifying subspaces using trial-averaged data (**Fig. 5a**), neural activity was first trial-averaged within trial type. Activity across trial types was then concatenated, providing a matrix $\mathbf{X} \in \square^{(T*C) \times N}$, where T is the number of time bins, C the number of trial types, and N the number of units. Trial-averaged neural activity was soft-normalized, then mean-centered as described in ref[40]. The matrix $\mathbf{X}$ was further divided into two matrices, $\mathbf{X}_{null}$ and $\mathbf{X}_{potent}$. $\mathbf{X}_{null}$ contained activity from [-1,0] seconds relative to the go cue, and $\mathbf{X}_{potent}$ [0,1] seconds relative to the go cue. Null and potent subspaces were then identified by solving the following optimization problem:

$$\left[\hat{\boldsymbol{Q}}_{null}, \hat{\boldsymbol{Q}}_{potent}\right] = argmax_{[\boldsymbol{Q}_{null}, \boldsymbol{Q}_{potent}]} \ \frac{1}{2}\frac{Tr\left(\boldsymbol{Q}_{null}^T \boldsymbol{C}_{null} \boldsymbol{Q}_{null}\right)}{\sum_{i=1}^{d_{null}} \sigma_{null}(i)} + \frac{1}{2}\frac{Tr\left(\boldsymbol{Q}_{potent}^T \boldsymbol{C}_{potent} \boldsymbol{Q}_{potent}\right)}{\sum_{i=1}^{d_{potent}} \sigma_{potent}(i)}$$

$$subject\ to \quad \boldsymbol{Q}_{null}^T \boldsymbol{Q}_{potent} = 0, \qquad \boldsymbol{Q}_{null}^T \boldsymbol{Q}_{null} = I, \qquad \boldsymbol{Q}_{potent}^T \boldsymbol{Q}_{potent} = I$$

where $\mathbf{C}_{null}$ and $\mathbf{C}_{potent}$ are the covariances of $\mathbf{X}_{null}$ and $\mathbf{X}_{potent}$, σ_{null} and σ_{potent} are the singular values of $\mathbf{C}_{null}$ and $\mathbf{C}_{potent}$, and d_{null} and d_{potent} are the dimensionality of the subspaces. This optimization problem jointly identifies null and potent subspaces that maximize the variance explained during the delay (null) and response (potent) epochs. The dimensionality of each space was chosen to be half the number of simultaneously recorded neurons, or twenty, whichever was smaller. Therefore, the dimensionality of the full population was equal to the dimensionality of the null or potent subspaces for sessions containing forty or fewer neurons. We capped dimensionality of subspaces at twenty for computational tractability. Optimization was performed using the manopt[105] toolbox for MATLAB.

For identifying subspaces using single-trial data (**Fig 5h**), single-trial neural activity was first binned in 5 ms intervals and smoothed with a causal Gaussian kernel with an s.d. of 35 ms. $\mathbf{X}_{null} \in \square^{(T_n*K) \times N}$ and $\mathbf{X}_{potent} \in \square^{(T_p*K) \times N}$ were defined using the single trial neural activity when the animal was stationary or moving (see ***Motion Energy***), respectively. T_n is the number of time bins annotated as the animal being stationary, T_p the number of time points annotated as the animal moving, and K the number of trials used for subspace identification. All correct and error trials from DR and WC contexts were used unless specified otherwise. Once the data was partitioned into moving and stationary time points, subspace identification was carried out as described for trial-averaged data.

Our decision to use binned and smoothed single-trial firing rates rather than inferring smooth single-trial firing rates using techniques such as FA, GPFA[73] and LFADS[74] came from the observation that, when using these techniques, an additional mode of dynamics not present in the original data was observed. To prevent our results

from being biased by the technique used to pre-process single-trial firing rates, we opted to used binned and smoothed data instead.

We quantified the normalized variance explained in a subspace as in refs[40,106] (**Fig. 5d,k**):

$$normVE = \frac{Tr(\boldsymbol{Q}^T \boldsymbol{C} \boldsymbol{Q})}{\sum_{i=1}^{d} \sigma(i)}$$

where **Q** is the subspace, **C** is the covariance of neural activity, and σ are the singular values of **C**. This normalization provides the maximum variance that can be captured by *d* dimensions.

Single units were reconstructed from null and potent subspaces according to the following equation:

$$\boldsymbol{X}_{recon} = \boldsymbol{X}_{subspace} \boldsymbol{Q}$$

where $\mathbf{X}_{\text{recon}}$ is the reconstructed neural activity, $\mathbf{X}_{\text{subspace}}$ is the projected neural activity within the null or potent subspace, and **Q** is either the null or potent subspace.

Coding directions within null and potent subspaces were obtained by projecting $\mathbf{X}_{\text{recon}}$ along coding directions obtained from the full neural population (**Fig. 7**).

To ask whether null and potent subspaces independently contained dynamics similar to that captured by coding directions, but along a different direction contained wholly within one subspace, we separately identified coding directions from null and potent subspace activity ($\boldsymbol{X}_{subspace}$). Activity within each subspace was then projected along the respective coding directions (**EDFig. 5b,c**).

Subspace alignment for an individual unit was calculated as:

$$A = \frac{VE_{null} - VE_{potent}}{VE_{null} + VE_{potent}}$$

where VE is the variance explained of each individual unit by the null or potent subspace, or by the activity along a coding direction within the null or potent subspace. VE for a single unit was calculated as:

$$R^2 \,/\, VE = 1 - \frac{\sum_t (\boldsymbol{x}_t - \hat{\boldsymbol{x}}_t)^2}{\sum_t (\boldsymbol{x}_t - \bar{\boldsymbol{x}})^2}$$

where x_t is the trial-averaged firing rate, $\hat{\boldsymbol{x}}$ the reconstructed trial-averaged firing rate, and *t* the time bin.

To ask if the subspace alignment distributions were different than expected by chance, we compared the distributions to those obtained from null and potent subspaces sampled randomly as described in ref [40]. Each element comprising a subspace were randomly sampled from a normal distribution with zero mean and unit variance but were biased by the covariance structure of the neural activity for a given session. Neural activity from each session was projected along the randomly sampled subspaces and alignment indices were calculated. This procedure was repeated 1000 times to generate null distributions (**EDFig. 4)**.

Subspaces were identified using data from DR and WC correct and error trials (**Fig. 5,7,8**). Control analyses were performed using separate sets of trials to assess if the potent subspace erroneously contained null-subspace dynamics. First, we estimated subspaces using WC trials only (**EDFig. 3, 5**). Second, we estimated subspaces using DR and WC trials, but restricted time points used to those in the response epoch only (**ED Fig. 3,5**). Both controls allowed us to estimate null and potent subspaces in the presence of uninstructed movements, but in the absence of planning dynamics. These controls thus allowed us to measure the degree to which the potent subspace erroneously captured null dynamics.

$CD_{Context}$ selectivity on 'Move' vs. 'Quiet' trials

For each session, DR and WC trials were first separated into 'Move' and 'Quiet' trials. 'Move' trials were those where the average motion energy in the ITI was greater than the movement threshold for that session, 'Quiet' trials were those where it was lower than the movement threshold. The last 40 trials in each session were excluded from analysis to account for the decrease in uninstructed movements that are observed towards the end of behavioral sessions as animals become sated and disengaged. 50% of 'Move' trials and 50% of 'Quiet' trials were randomly sampled from DR and WC trials separately to ensure that 'Move' and 'Quiet' trials did not contain an overrepresentation of one context. These trials were then pooled together and used to calculate $CD_{Context}$ (fit trials). Population activity from the remaining 'Move' and 'Quiet' trials (test trials) was then projected along $CD_{Context}$. Selectivity was defined as the trial-averaged projection along $CD_{Context}$ on DR – WC trials (**Fig. 8b**).

Hierarchical bootstrapping

Projections along coding directions were obtained via a hierarchical bootstrapping procedure[107,108] (**Figs. 2, 7** and **EDFigs. 3, 4, 5)**. Pseudopopulations were constructed by randomly sampling with replacement M mice, 2 sessions per sampled mouse, 50 correct trials of each type, 20 error trials of each type, and 20 neurons. M is the number of mice in the original cohort. Bootstrapping was repeated for 1000 iterations. For all figures, mean and 95% confidence intervals (shaded area) of the bootstrap distribution are shown. For selectivity, 5-95% confidence intervals are shown to indicate where projections significantly differ from zero ($p<0.05$, one-sided test, bootstrap).

Statistics

No statistical methods were used to determine sample sizes. All two-sample *t*-tests were Students *t*-tests. All *t*-tests were two-sided unless stated otherwise.

DATA AVAILABILITY

Primary and derived data described in this study will be made available on Figshare upon publication.

CODE AVAILABILITY

MATLAB code for subspace identification is available at https://github.com/economolab/subspaceID. Custom MATLAB code used for analyses will be made available on Github upon publication.

COMPETING INTERESTS

The authors declare no competing interests.

AUTHOR CONTRIBUTIONS

MAH, JEB, and MNE conceived of the project. MNE and CC supervised research. MAH, JEB, and MNE designed experiments. MAH, JEB, JLUN, and EKH performed experiments. MAH, JEB, and MNE analyzed data. MAH, JEB, CC, and MNE wrote the manuscript.

ACKNOWLEDGMENTS

The authors thank, Karel Svoboda, Brian DePasquale, Shaul Druckmann, and Ben Scott for helpful discussions. We thank Tim Wang for helpful comments on the manuscript. This work was supported by the Whitehall Foundation, the Klingenstein Fund, the Simons Foundation, and NIH R01NS121409.

References

1. Alexander, G. E. & Crutcher, M. D. Neural representations of the target (goal) of visually guided arm movements in three motor areas of the monkey. *Journal of Neurophysiology* **64**, 164–178 (1990).
2. Cisek, P. & Kalaska, J. F. Neural Correlates of Reaching Decisions in Dorsal Premotor Cortex: Specification of Multiple Direction Choices and Final Selection of Action. *Neuron* **45**, 801–814 (2005).

3. Lebedev, M. A. & Wise, S. P. Insights into Seeing and Grasping: Distinguishing the Neural Correlates of Perception and Action. *Behavioral and Cognitive Neuroscience Reviews* **1**, 108–129 (2002).

4. Chandrasekaran, C., Peixoto, D., Newsome, W. T. & Shenoy, K. V. Laminar differences in decision-related neural activity in dorsal premotor cortex. *Nat Commun* **8**, 614 (2017).

5. Chen, S. *et al*. Brain-wide neural activity underlying memory-guided movement. 2023.03.01.530520 Preprint at https://doi.org/10.1101/2023.03.01.530520 (2023).

6. Basso, M. A. & May, P. J. Circuits for Action and Cognition: A View from the Superior Colliculus. *Annu Rev Vis Sci* **3**, 197–226 (2017).

7. Zimnik, A. J. & Churchland, M. M. Independent generation of sequence elements by motor cortex. *Nat Neurosci* **24**, 412–424 (2021).

8. Ames, K. C., Ryu, S. I. & Shenoy, K. V. Simultaneous motor preparation and execution in a last-moment reach correction task. *Nat Commun* **10**, 2718 (2019).

9. Flash, T. & Henis, E. Arm Trajectory Modifications During Reaching Towards Visual Targets. *Journal of Cognitive Neuroscience* **3**, 220–230 (1991).

10. Fuster, J. M. & Alexander, G. E. Neuron activity related to short-term memory. *Science* **173**, 652–654 (1971).

11. Romo, R., Brody, C. D., Hernández, A. & Lemus, L. Neuronal correlates of parametric working memory in the prefrontal cortex. *Nature* **399**, 470–473 (1999).

12. Erlich, J. C., Bialek, M. & Brody, C. D. A Cortical Substrate for Memory-Guided Orienting in the Rat. *Neuron* **72**, 330–343 (2011).

13. Tanji, J. & Evarts, E. V. Anticipatory activity of motor cortex neurons in relation to direction of an intended movement. *Journal of Neurophysiology* **39**, 1062–1068 (1976).

14. Guo, Z. V. *et al.* Flow of Cortical Activity Underlying a Tactile Decision in Mice. *Neuron* **81**, 179–194 (2014).

15. Wallis, J. D., Anderson, K. C. & Miller, E. K. Single neurons in prefrontal cortex encode abstract rules. *Nature* **411**, 953–956 (2001).

16. Mante, V., Sussillo, D., Shenoy, K. V. & Newsome, W. T. Context-dependent computation by recurrent dynamics in prefrontal cortex. *Nature* **503**, 78–84 (2013).

17. Schultz, W., Dayan, P. & Montague, P. R. A Neural Substrate of Prediction and Reward. *Science* **275**, 1593–1599 (1997).

18. Watabe-Uchida, M., Eshel, N. & Uchida, N. Neural Circuitry of Reward Prediction Error. *Annual Review of Neuroscience* **40**, 373–394 (2017).

19. Freedman, D. J., Riesenhuber, M., Poggio, T. & Miller, E. K. Categorical representation of visual stimuli in the primate prefrontal cortex. *Science* **291**, 312–316 (2001).

20. Carr, M. F., Jadhav, S. P. & Frank, L. M. Hippocampal replay in the awake state: a potential substrate for memory consolidation and retrieval. *Nat Neurosci* **14**, 147–153 (2011).

21. Levy, S. *et al.* Cell-Type-Specific Outcome Representation in the Primary Motor Cortex. *Neuron* **107**, 954-971.e9 (2020).

22. Padoa-Schioppa, C. & Assad, J. A. Neurons in Orbitofrontal Cortex Encode Economic Value. *Nature* **441**, 223–226 (2006).

23. Zagha, E. The Importance of Accounting for Movement When Relating Neuronal Activity to Sensory and Cognitive Processes | Journal of Neuroscience. https://www.jneurosci.org/content/42/8/1375#ref-90 (2022).

24. Drew, P. J., Winder, A. T. & Zhang, Q. Twitches, Blinks, and Fidgets: Important Generators of Ongoing Neural Activity. *Neuroscientist* **25**, 298–313 (2019).

25. Galton, F. The Measure of Fidget. *Nature* **32**, 174–175 (1885).

26. Hulsey, D., Zumwalt, K., Mazzucato, L., McCormick, D. A. & Jaramillo, S. Decision-making dynamics are predicted by arousal and uninstructed movements. 2023.03.02.530651 Preprint at https://doi.org/10.1101/2023.03.02.530651 (2023).

27. Tremblay, S., Testard, C., DiTullio, R. W., Inchauspé, J. & Petrides, M. Neural cognitive signals during spontaneous movements in the macaque. *Nat Neurosci* **26**, 295–305 (2023).

28. Hafed, Z. M., Lovejoy, L. P. & Krauzlis, R. J. Modulation of Microsaccades in Monkey during a Covert Visual Attention Task. *J Neurosci* **31**, 15219–15230 (2011).

29. Corneil, B. D., Munoz, D. P., Chapman, B. B., Admans, T. & Cushing, S. L. Neuromuscular consequences of reflexive covert orienting. *Nat Neurosci* **11**, 13–15 (2008).

30. Musall, S., Kaufman, M. T., Juavinett, A. L., Gluf, S. & Churchland, A. K. Single-trial neural dynamics are dominated by richly varied movements. *Nat Neurosci* **22**, 1677–1686 (2019).

31. Stringer, C. Spontaneous behaviors drive multidimensional, brainwide activity | Science. https://www.science.org/doi/10.1126/science.aav7893 (2019).

32. Steinmetz, N. A., Zatka-Haas, P., Carandini, M. & Harris, K. D. Distributed coding of choice, action and engagement across the mouse brain. *Nature* **576**, 266–273 (2019).

33. Mangin, E. N., Chen, J., Lin, J. & Li, N. Behavioral measurements of motor readiness in mice. 2023.02.03.527054 Preprint at https://doi.org/10.1101/2023.02.03.527054 (2023).

34. Terada, S.-I., Kobayashi, K. & Matsuzaki, M. Transition of distinct context-dependent ensembles from secondary to primary motor cortex in skilled motor performance. *Cell Reports* **41**, 111494 (2022).

35. Lowet, E. *et al.* Enhanced Neural Processing by Covert Attention only during Microsaccades Directed toward the Attended Stimulus. *Neuron* **99**, 207-214.e3 (2018).

36. Popescu, S. T. & Wexler, M. Spontaneous Body Movements in Spatial Cognition. *Front Psychol* **3**, 136 (2012).

37. Hajnal, J. V. *et al.* Artifacts due to stimulus correlated motion in functional imaging of the brain. *Magn Reson Med* **31**, 283–291 (1994).

38. Dominiak, S. E. *et al.* Whisking Asymmetry Signals Motor Preparation and the Behavioral State of Mice. *J. Neurosci.* **39**, 9818–9830 (2019).

39. Kaufman, M. T., Churchland, M. M., Ryu, S. I. & Shenoy, K. V. Cortical activity in the null space: permitting preparation without movement. *Nat Neurosci* **17**, 440–448 (2014).

40. Elsayed, G. F., Lara, A. H., Kaufman, M. T., Churchland, M. M. & Cunningham, J. P. Reorganization between preparatory and movement population responses in motor cortex. *Nat Commun* **7**, 13239 (2016).

41. Liu, T. T., Nalci, A. & Falahpour, M. The global signal in fMRI: Nuisance or Information? *NeuroImage* **150**, 213–229 (2017).

42. Friston, K. J., Williams, S., Howard, R., Frackowiak, R. S. J. & Turner, R. Movement-Related effects in fMRI time-series. *Magnetic Resonance in Medicine* **35**, 346–355 (1996).

43. Bullmore, E. T. *et al.* Methods for diagnosis and treatment of stimulus correlated motion in generic brain activation studies using fMRI. *Hum Brain Mapp* **7**, 38–48 (1998).

44. Power, J. D., Schlaggar, B. L. & Petersen, S. E. Recent progress and outstanding issues in motion correction in resting state fMRI. *NeuroImage* **0**, 536 (2015).

45. Cisek, P. & Kalaska, J. F. Neural Mechanisms for Interacting with a World Full of Action Choices. *Annual Review of Neuroscience* **33**, 269–298 (2010).

46. Cisek, P. & Pastor-Bernier, A. On the challenges and mechanisms of embodied decisions. *Philosophical Transactions of the Royal Society B: Biological Sciences* **369**, 20130479 (2014).

47. Koay, S. A., Charles, A. S., Thiberge, S. Y., Brody, C. D. & Tank, D. W. Sequential and efficient neural-population coding of complex task information. *Neuron* **110**, 328-349.e11 (2022).

48. Aoi, M. C., Mante, V. & Pillow, J. W. Prefrontal cortex exhibits multidimensional dynamic encoding during decision-making. *Nat Neurosci* **23**, 1410–1420 (2020).

49. Hennig, J. A. *et al.* Learning is shaped by abrupt changes in neural engagement. *Nat Neurosci* **24**, 727–736 (2021).

50. Druckmann, S. & Chklovskii, D. B. Neuronal Circuits Underlying Persistent Representations Despite Time Varying Activity. *Current Biology* **22**, 2095–2103 (2012).

51. Galiñanes, G. L., Bonardi, C. & Huber, D. Directional Reaching for Water as a Cortex-Dependent Behavioral Framework for Mice. *Cell Reports* **22**, 2767–2783 (2018).

52. Mathis, A. *et al.* DeepLabCut: markerless pose estimation of user-defined body parts with deep learning. *Nat Neurosci* **21**, 1281–1289 (2018).

53. Mayrhofer, J. M. *et al.* Distinct Contributions of Whisker Sensory Cortex and Tongue-Jaw Motor Cortex in a Goal-Directed Sensorimotor Transformation. *Neuron* **103**, 1034-1043.e5 (2019).

54. Inagaki, H. K. *et al.* Neural Algorithms and Circuits for Motor Planning. *Annual Review of Neuroscience* **45**, 249–271 (2022).

55. Xu, D. *et al.* Cortical processing of flexible and context-dependent sensorimotor sequences. *Nature* **603**, 464–469 (2022).

56. Chen, T.-W., Li, N., Daie, K. & Svoboda, K. A Map of Anticipatory Activity in Mouse Motor Cortex. *Neuron* **94**, 866-879.e4 (2017).

57. Yin, X., Wang, Y., Li, J. & Guo, Z. V. Lateralization of short-term memory in the frontal cortex. *Cell Reports* **40**, 111190 (2022).

58. Li, N., Chen, T.-W., Guo, Z. V., Gerfen, C. R. & Svoboda, K. A motor cortex circuit for motor planning and movement. *Nature* **519**, 51–56 (2015).

59. Esmaeili, V. *et al.* Rapid suppression and sustained activation of distinct cortical regions for a delayed sensory-triggered motor response. *Neuron* **109**, 2183-2201.e9 (2021).

60. Li, N., Daie, K., Svoboda, K. & Druckmann, S. Robust neuronal dynamics in premotor cortex during motor planning. *Nature* **532**, 459–464 (2016).

61. Yang, W., Tipparaju, S. L., Chen, G. & Li, N. Thalamus-driven functional populations in frontal cortex support decision-making. *Nat Neurosci* **25**, 1339–1352 (2022).

62. Economo, M. N. *et al.* Distinct descending motor cortex pathways and their roles in movement. *Nature* **563**, 79–84 (2018).

63. Svoboda, K. & Li, N. Neural mechanisms of movement planning: motor cortex and beyond. *Current Opinion in Neurobiology* **49**, 33–41 (2018).

64. Inagaki, H. K., Fontolan, L., Romani, S. & Svoboda, K. Discrete attractor dynamics underlies persistent activity in the frontal cortex. *Nature* **566**, 212–217 (2019).

65. Shenoy, K. V., Sahani, M. & Churchland, M. M. Cortical Control of Arm Movements: A Dynamical Systems Perspective. *Annual Review of Neuroscience* **36**, 337–359 (2013).

66. Orlandi, J. G., Abdolrahmani, M., Aoki, R., Lyamzin, D. R. & Benucci, A. Distributed context-dependent choice information in mouse posterior cortex. *Nat Commun* **14**, 192 (2023).

67. Inagaki, H. K., Inagaki, M., Romani, S. & Svoboda, K. Low-Dimensional and Monotonic Preparatory Activity in Mouse Anterior Lateral Motor Cortex. *J. Neurosci.* **38**, 4163–4185 (2018).

68. Finkelstein, A. *et al.* Attractor dynamics gate cortical information flow during decision-making. *Nat Neurosci* **24**, 843–850 (2021).

69. Narayanan, N. S. Ramping activity is a cortical mechanism of temporal control of action. *Current Opinion in Behavioral Sciences* **8**, 226–230 (2016).

70. Cisek, P., Puskas, G. A. & El-Murr, S. Decisions in Changing Conditions: The Urgency-Gating Model. *J. Neurosci.* **29**, 11560–11571 (2009).

71. Tanaka, M. Cognitive Signals in the Primate Motor Thalamus Predict Saccade Timing. *J. Neurosci.* **27**, 12109–12118 (2007).

72. Maimon, G. & Assad, J. A. A cognitive signal for the proactive timing of action in macaque LIP. *Nat Neurosci* **9**, 948–955 (2006).

73. Yu, B. M. *et al.* Gaussian-Process Factor Analysis for Low-Dimensional Single-Trial Analysis of Neural Population Activity. *Journal of Neurophysiology* **102**, 614–635 (2009).

74. Pandarinath, C. *et al.* Inferring single-trial neural population dynamics using sequential auto-encoders. *Nat Methods* **15**, 805–815 (2018).

75. Kawai, R. *et al.* Motor cortex is required for learning but not for executing a motor skill. *Neuron* **86**, 800–812 (2015).

76. Safaie, M. *et al.* Turning the body into a clock: Accurate timing is facilitated by simple stereotyped interactions with the environment. *Proceedings of the National Academy of Sciences* **117**, 13084–13093 (2020).

77. Moore, J. D., Kleinfeld, D. & Wang, F. How the brainstem controls orofacial behaviors comprised of rhythmic actions. *Trends in Neurosciences* **37**, 370–380 (2014).

78. Arber, S. & Costa, R. M. Networking brainstem and basal ganglia circuits for movement. *Nat Rev Neurosci* **23**, 342–360 (2022).

79. Merel, J., Botvinick, M. & Wayne, G. Hierarchical motor control in mammals and machines. *Nat Commun* **10**, 5489 (2019).

80. Hausmann, S. B., Vargas, A. M., Mathis, A. & Mathis, M. W. Measuring and modeling the motor system with machine learning. *Current Opinion in Neurobiology* **70**, 11–23 (2021).

81. Pereira, T. D., Shaevitz, J. W. & Murthy, M. Quantifying behavior to understand the brain. *Nat Neurosci* **23**, 1537–1549 (2020).

82. Anderson, D. J. & Perona, P. Toward a Science of Computational Ethology. *Neuron* **84**, 18–31 (2014).

83. Miller, C. T. *et al.* Natural behavior is the language of the brain. *Current Biology* **32**, R482–R493 (2022).

84. Krakauer, J. W., Ghazanfar, A. A., Gomez-Marin, A., MacIver, M. A. & Poeppel, D. Neuroscience Needs Behavior: Correcting a Reductionist Bias. *Neuron* **93**, 480–490 (2017).

85. Datta, S. R., Anderson, D. J., Branson, K., Perona, P. & Leifer, A. Computational Neuroethology: A Call to Action. *Neuron* **104**, 11–24 (2019).

86. Parker, P. R. L., Brown, M. A., Smear, M. C. & Niell, C. M. Movement-Related Signals in Sensory Areas: Roles in Natural Behavior. *Trends in Neurosciences* **43**, 581–595 (2020).

87. Gomez-Marin, A. & Ghazanfar, A. A. The Life of Behavior. *Neuron* **104**, 25–36 (2019).

88. Dennis, E. J. *et al.* Systems Neuroscience of Natural Behaviors in Rodents. *J. Neurosci.* **41**, 911–919 (2021).

89. Testard, C. *et al.* Neural signatures of natural behavior in socializing macaques. 2023.07.05.547833 Preprint at https://doi.org/10.1101/2023.07.05.547833 (2023).

90. Marshall, J. D. *et al.* Continuous Whole-Body 3D Kinematic Recordings across the Rodent Behavioral Repertoire. *Neuron* **109**, 420-437.e8 (2021).

91. Christensen, A. J., Ott, T. & Kepecs, A. Cognition and the single neuron: How cell types construct the dynamic computations of frontal cortex. *Current Opinion in Neurobiology* **77**, 102630 (2022).

92. Wang, Z. A. *et al.* Not everything, not everywhere, not all at once: a study of brain-wide encoding of movement. 2023.06.08.544257 Preprint at https://doi.org/10.1101/2023.06.08.544257 (2023).

93. Gallego, J. A., Perich, M. G., Miller, L. E. & Solla, S. A. Neural Manifolds for the Control of Movement. *Neuron* **94**, 978–984 (2017).

94. Fortunato, C. *et al.* Nonlinear manifolds underlie neural population activity during behaviour. 2023.07.18.549575 Preprint at https://doi.org/10.1101/2023.07.18.549575 (2023).

95. Dahmen, D. *et al.* Strong and localized recurrence controls dimensionality of neural activity across brain areas. 2020.11.02.365072 Preprint at https://doi.org/10.1101/2020.11.02.365072 (2023).

96. Morales-Gregorio, A. *et al.* Neural manifolds in V1 change with top-down signals from V4 targeting the foveal region. 2023.06.14.544966 Preprint at https://doi.org/10.1101/2023.06.14.544966 (2023).

97. Sohn, H., Narain, D., Meirhaeghe, N. & Jazayeri, M. Bayesian Computation through Cortical Latent Dynamics. *Neuron* **103**, 934-947.e5 (2019).

98. Joshi, S. & Gold, J. I. Pupil Size as a Window on Neural Substrates of Cognition. *Trends in Cognitive Sciences* **24**, 466–480 (2020).

99. Lee, C. R. & Margolis, D. J. Pupil Dynamics Reflect Behavioral Choice and Learning in a Go/NoGo Tactile Decision-Making Task in Mice. *Frontiers in Behavioral Neuroscience* **10**, (2016).

100. Bradley, M. M., Miccoli, L., Escrig, M. A. & Lang, P. J. The pupil as a measure of emotional arousal and autonomic activation. *Psychophysiology* **45**, 602–607 (2008).

101. Yin, C. *et al.* Engaged decision-makers align spontaneous movements to stereotyped task demands. 2023.06.26.546404 Preprint at https://doi.org/10.1101/2023.06.26.546404 (2023).

102. Kim, T. H. *et al.* Long-Term Optical Access to an Estimated One Million Neurons in the Live Mouse Cortex. *Cell Reports* **17**, 3385–3394 (2016).

103. Jun, J. J. *et al.* Fully integrated silicon probes for high-density recording of neural activity. *Nature* **551**, 232–236 (2017).

104. Jun, J. J. *et al.* Real-time spike sorting platform for high-density extracellular probes with ground-truth validation and drift correction. *bioRxiv* 101030 (2017) doi:10.1101/101030.

105. Boumal, N., Mishra, B., Absil, P.-A. & Sepulchre, R. Manopt, a Matlab Toolbox for Optimization on Manifolds. *Journal of Machine Learning Research* **15**, 1455–1459 (2014).

106. Jiang, X., Saggar, H., Ryu, S. I., Shenoy, K. V. & Kao, J. C. Structure in Neural Activity during Observed and Executed Movements Is Shared at the Neural Population Level, Not in Single Neurons. *Cell Reports* **32**, 108006 (2020).

107. Aarts, E., Verhage, M., Veenvliet, J. V., Dolan, C. V. & van der Sluis, S. A solution to dependency: using multilevel analysis to accommodate nested data. *Nat Neurosci* **17**, 491–496 (2014).

108. de Leeuw, J. & Meijer, E. *Handbook of Multilevel Analysis*. vols 401–433 (Springer, New York, 2008).

Extended Data

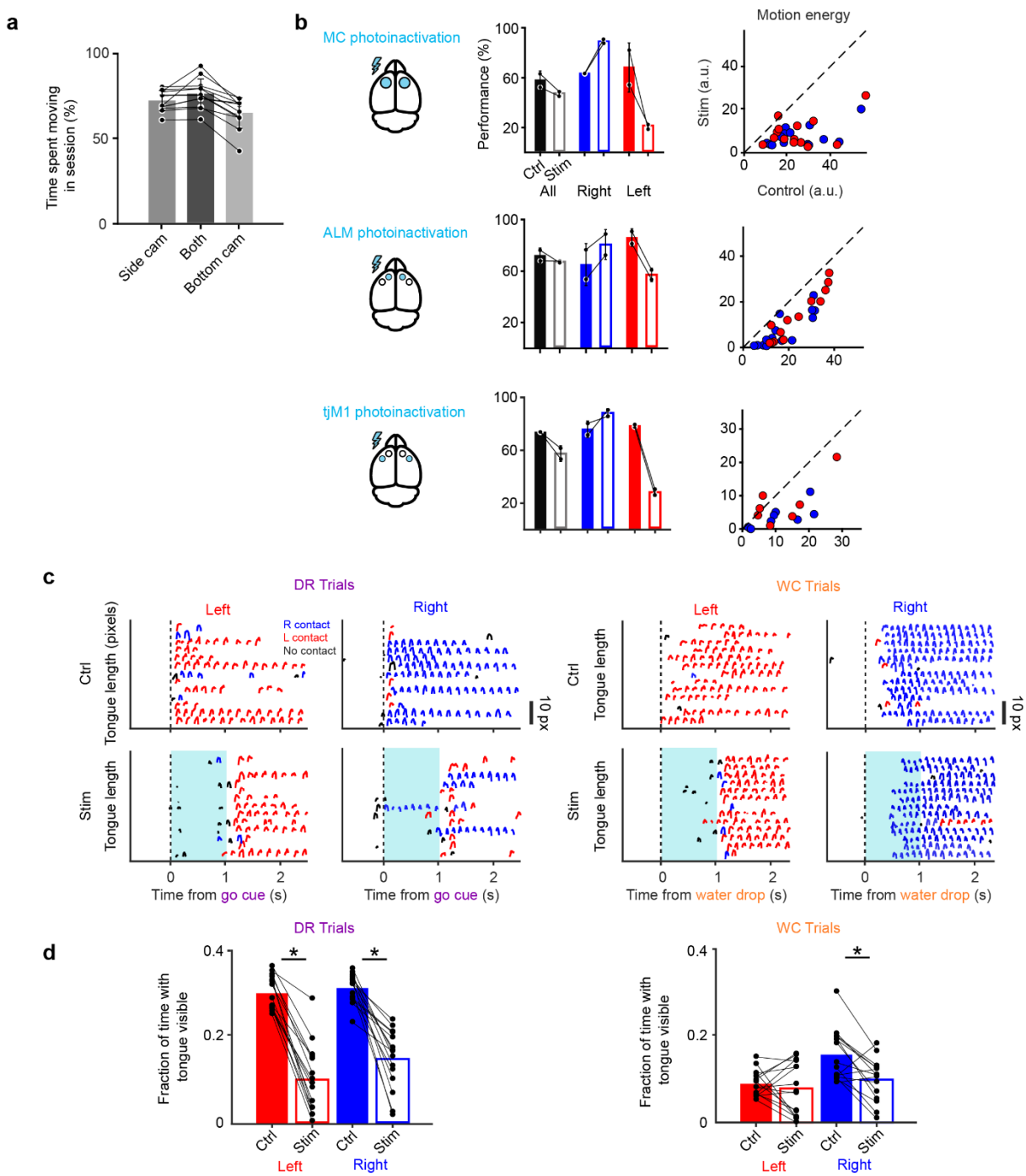

Extended Data Fig. 1 – Effects of photoinactivation of ALM and tjM1 on uninstructed movements and tongue kinematics. a. Percentage of time spent moving (see **Methods**) in a session determined by video recordings using the side view, bottom view, and both views. Points indicate each of the 12 randomly selected sessions used for this analysis. **b.** Delay epoch photoinactivation results are not exclusive to full MC photoinactivation (*top*, copied from **Fig. 1g-i,** n=2 mice, 14 sessions). Similar results were obtained when photoinactiving ALM (*middle*, n=2 mice, 15 sessions) and tjM1 (*bottom*, n=2 mice, 9 sessions) photoinactivation. **c.** Tongue length during control and go cue photoinactivation trials for delayed-response (*left*) and water-cued (*right*) contexts. Blue traces indicate right lickport contacts, red traces indicate left contacts, and black traces indicate no contact. Vertical dashed line indicates go cue or water drop onset. Blue shaded region indicates photoinactivation period. **d.** Fraction of time with tongue visible during photoinactivation period for DR trials (*left*) and WC trials (*right*). Asterisks denote significant differences ($p < 0.01$) between control and photoinactivation trials (p-values from left to right: 1.017e-08, 2.030e-06, 0.481, 0.002; paired t-test).

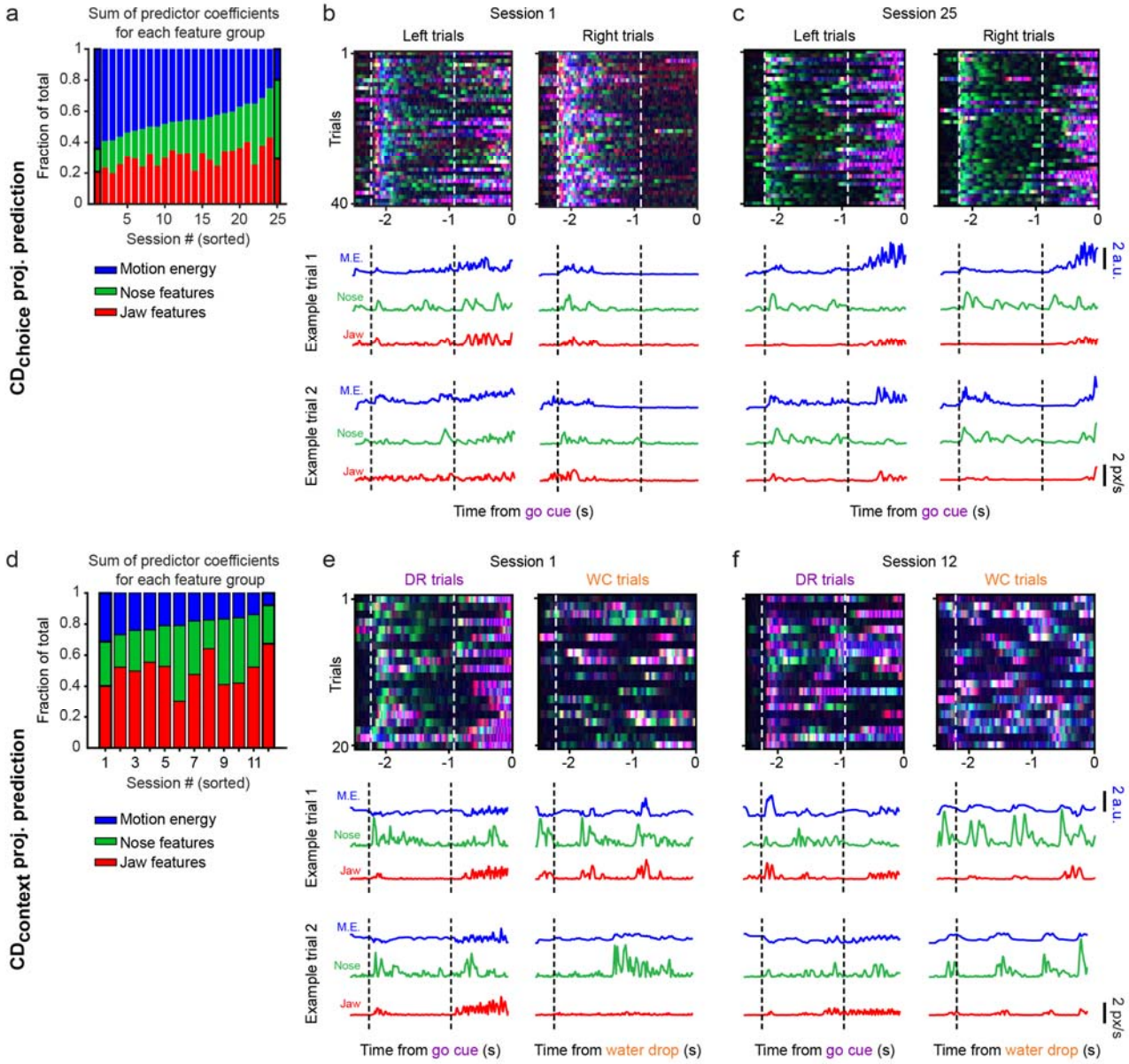

Extended Data Fig. 2 - Session-by-session variability of the relationship between kinematic features and putative cognitive dynamics. a. Regression weights for each group of kinematic predictors for predicting CD_{choice} projections, as a fraction of all predictor coefficients (see **Methods**). Sessions are sorted in descending order by motion energy fraction. Outlined bars indicate example sessions shown in (b-c). **b.** Example session of uninstructed movements where motion energy made up the largest fraction of regression weights for predicting CD_{choice} projections. *Top*, overlayed jaw/nose speed or motion energy for a subset trials. *Bottom*, two example trials of kinematic feature trajectories. **c.** Same as (b) but for an example session where jaw and nose features made up a larger fraction of regression weights. **d.** Same as (a) but for predicting $CD_{context}$ projections. **e, f.** Same as (b-c) but for two example sessions with different regression weight fractions for predicting $CD_{context}$ projections.

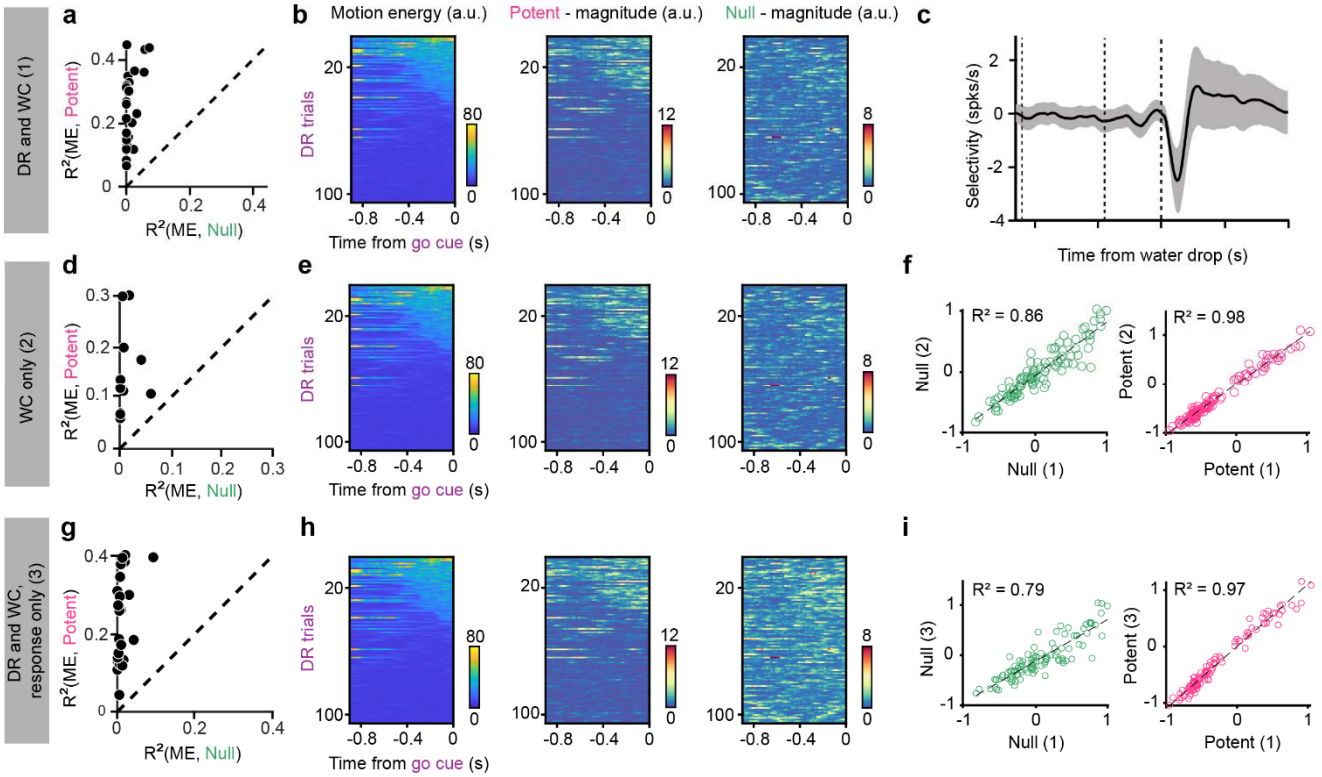

Extended Data Fig. 3 – Control analyses for subspace decomposition. a-b. Null and potent subspaces estimated as in **Fig. 5g-l** using DR and WC trials. **a.** Variance explained **(**R^2) of motion energy by the sum squared magnitude of activity in the null and potent subspaces on single trials. Each point is the mean across trials for a session. **b.** *Left*, motion energy on single trials for an example session. *Middle*, sum squared magnitude of activity in the potent subspace on single trials. *Right*, sum squared magnitude of activity in the null subspace. Trials sorted by average delay epoch motion energy. **c.** Selectivity (left vs. right) of the neural population during WC trials. Mean and 95% CI across sessions shown. **d-e.** Same as (a-b) but the null and potent subspaces have been estimated using WC trials only. This allows for the estimation of a "null" model of movements in the absence of goal-directed behavior. **f.** Normalized magnitude of activity in the null space (*left*) or potent space (*right*) when estimated using DR and WC trials versus when estimated using WC trials only. Circles are average activity per trial for an example session. **g-h.** Same as (a-b), but the null and potent subspaces have been estimated using data restricted to the response epoch of DR and WC trials. Only the delay epoch shown for (b,e,h) to highlight the methods ability to capture delay epoch uninstructed movements in the potent subspace under various subspace estimation conditions. **i.** Magnitude of activity in the null space (*left*) or potent space (*right*) when estimated using DR and WC trials versus when estimated using data from the response epoch of DR and WC trials. Circles are average activity per trial for an example session.

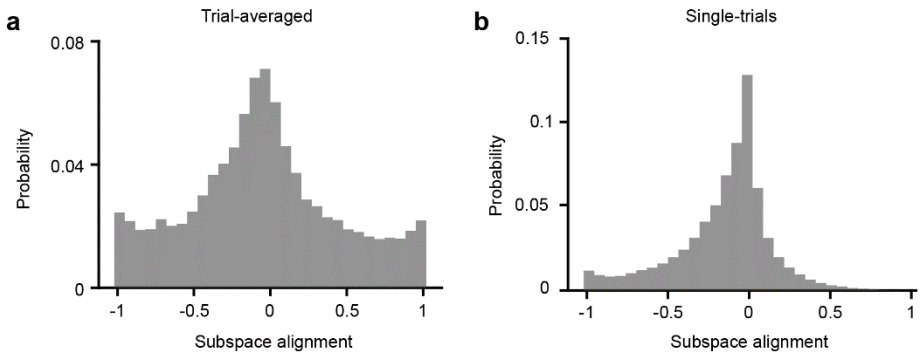

Extended Data Fig. 4 – Random subspaces show single units contribute both to null and potent subspaces. In order to ask whether the subspace alignment distributions seen in our data (**Fig. 5g,n**) were different from those expected by chance, we compared these distributions against alignment distributions obtained when neural activity is decomposed into random null and potent subspaces. Each element of the random subspaces was drawn from a normal distribution with zero mean and unit variance (see **Methods**). Null distributions of alignment indices are shown for **a.** trial-averaged data and **b.** single-trial data. Both alignment distributions differed from those obtained from random subspaces (Trial-averaged data, $p=6\text{x}10^{-8}$; Single-trial data, $p=6\text{x}10^{-9}$; two-sample Kolmogorov-Smirnov test).

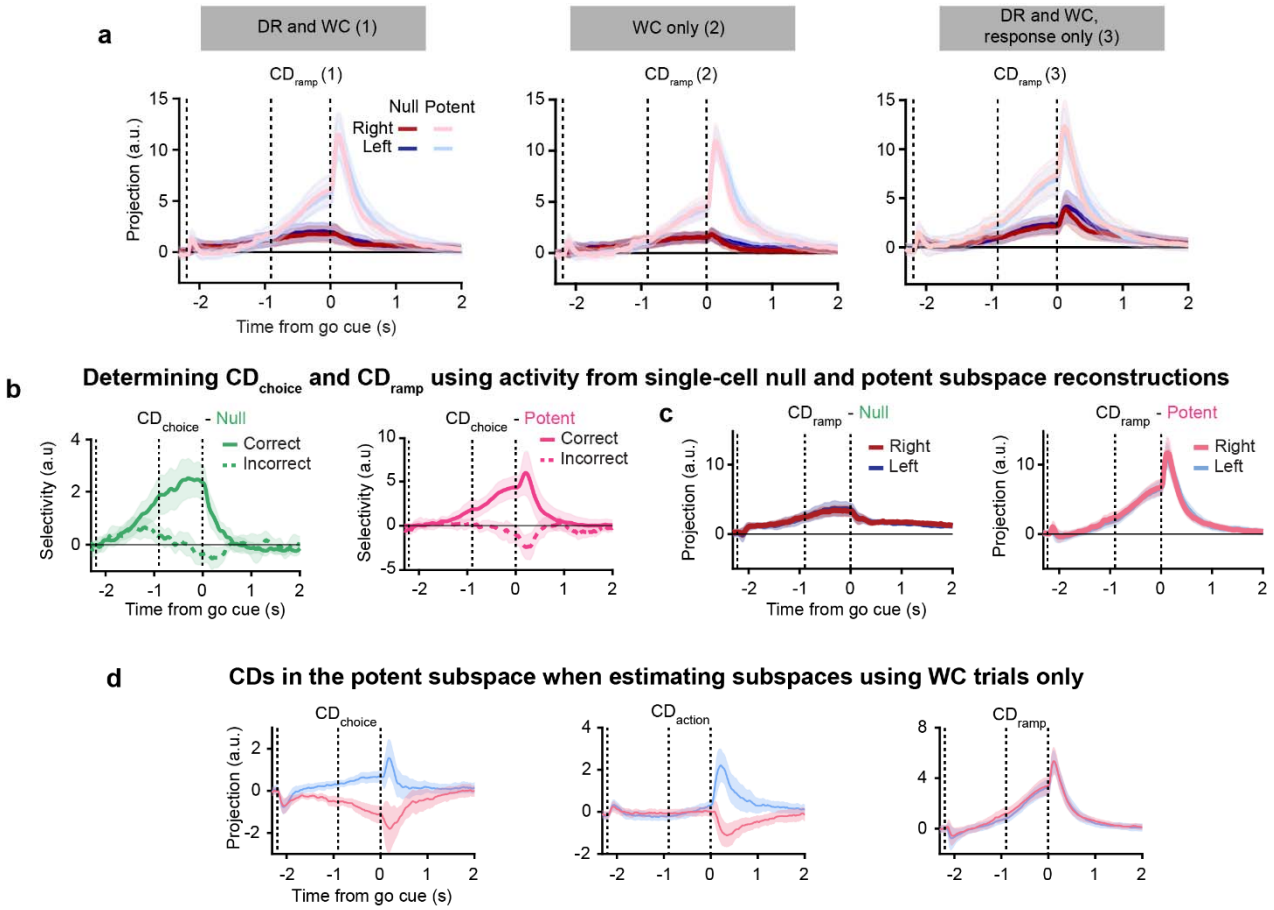

EDFigure 5 – Alternative procedure for estimating motor planning CDs from subspaces. a. Projections of null and potent subspace activity along CD_{ramp} for each of the three control conditions. Null and potent subspaces were identified using both DR and WC trials (*left*), WC trials only (*middle*), and the response epoch of DR and WC trials (*right*). Mean and 95% CI of bootstrap distribution shown. **b.** Selectivity in null (*left*) and potent (*right*) components of CDchoice projections when CDchoice is determined from subspace activity, rather than from the full neural population. Mean and 95% CI of bootstrap distribution shown. **c.** Projections along null (*left*) and potent (*right*) components of CDramp when CDramp is determined from subspace activity, rather than from the full neural population. Mean and 95% CI of bootstrap distribution shown. **d.** Projections of potent subspace activity along CDchoice, CDaction, and CDramp when determining subspaces from WC trials only. CDs were determined using the full neural population. Mean and 95% CI of bootstrap distribution shown.

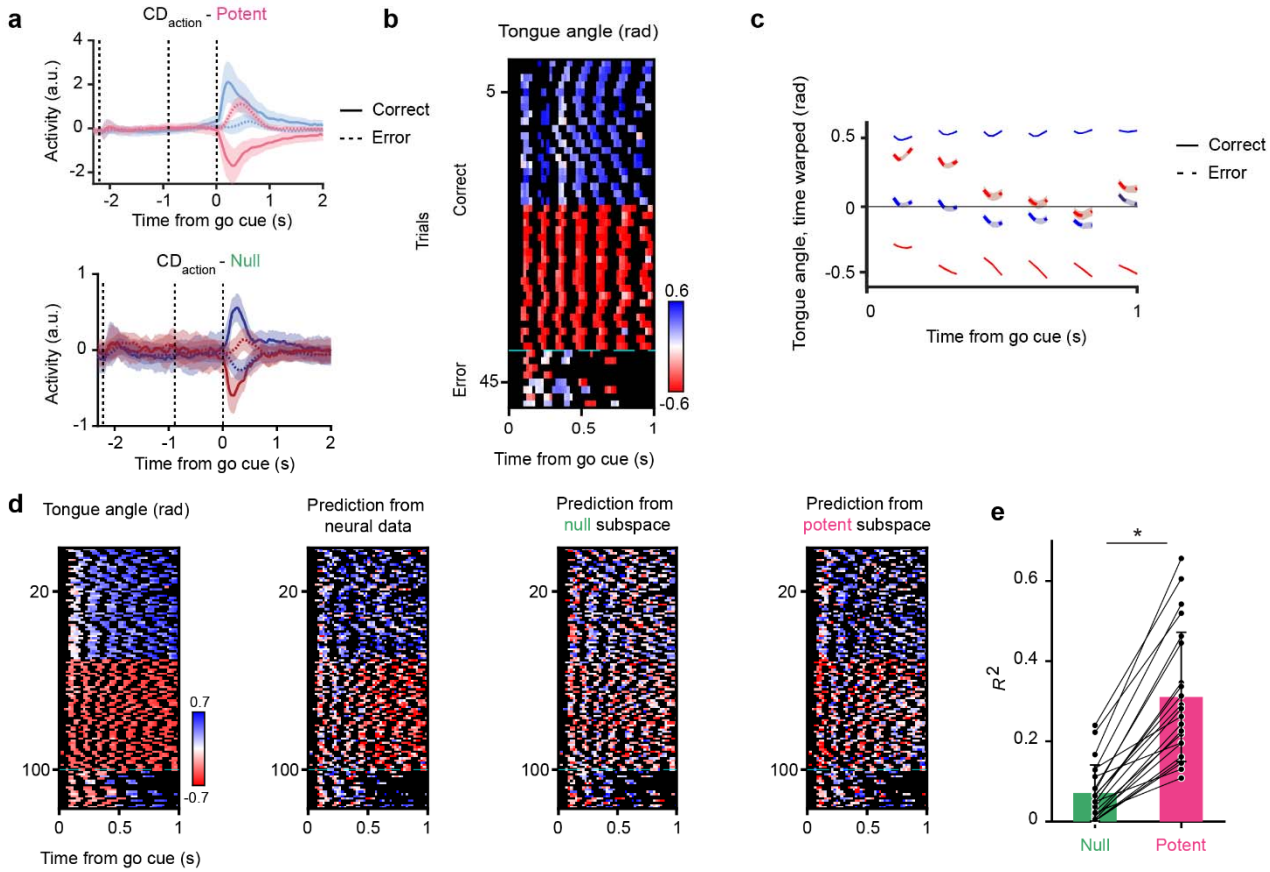

EDFigure 6 – Relationship between tongue angle and neural activity in the null and potent subspaces. a. Projections along potent (*top*) and null (*bottom*) components of CD_{action}. Correct trials shown in solid lines and error trials shown in dashed lines. **b.** Tongue angle for an example session for correct and error trials. **c.** Tongue angle on correct and error right and left trials. Tongue angle was linearly time warped to allow for averaging over trials and sessions. Mean and s.e.m. across sessions shown. **d.** Tongue angle (*left*) and predictions from the full population neural activity (*middle left*), null subspace activity (*middle right*), and potent subspace activity (*right*) for an example session. **e.** Variance explained (R^2) between tongue angle and predictions from null (*green*) and potent (pink) subspaces. Asterisks denote significant differences between predictions from null and potent subspaces (p=2 x10^{-8}, paired t-test).

Supplementary Movie 1 – Uninstructed movements vary in their identity and timing. Example trials in which uninstructed movements vary in their identity (across rows) and timing (across columns). Traces represent the y-position of the feature within the video frame. All example trials taken from the same mouse and session.